

Frequency Smoothed Robust Capon Beamformer Applied to Medical Ultrasound Imaging

Xian Long

B. Eng. (Honours)
Australian National University

July 2014

A THESIS SUBMITTED FOR THE DEGREE OF MASTER OF PHILOSOPHY
AT THE AUSTRALIAN NATIONAL UNIVERSITY



**Australian
National
University**

Applied Signal Processing Group
Research School of Engineering
College of Engineering and Computer Science
The Australian National University

Declaration

The contents of this thesis are the results of original research and have not been submitted for a higher degree to any other university or institution.

Much of the work in this thesis has been published or has been submitted for publication as journal papers or conference proceedings. In some cases, the conference papers contain overlapping material with the journal publications. The following is a list of these publications.

Journals

1. X. Long, S. M. A. Salehin, and T. D. Abhayapala, “Frequency Smoothed Robust Capon Beamformer with Frequency Compounding Applied to Medical Ultrasound Imaging,” submitted to IEEE Trans. on Ultrasonics, Ferroelectrics, and Frequency Control.

Conferences

1. X. Long, S. M. A. Salehin, and T. D. Abhayapala, “Robust Capon Beamformer with Frequency Smoothing Applied to Medical Ultrasound Imaging,” 2014 IEEE Workshop on Statistical Signal Processing (SSP), Gold Coast, Australia, Jul. 2014.

The research work presented in this thesis has been performed jointly with Dr. S. M. Akramus Salehin and Prof. Thushara D. Abhayapala. The substantial majority of this work was my own.

Xian Long
College of Engineering and Computer Science,
The Australian National University,
Canberra,
ACT 0200,
Australia.

Acknowledgements

The work presented in this thesis would not have been possible without the support of a number of individuals and organizations and they are gratefully acknowledged below.

I am grateful to Prof. Thushara D. Abhayapala and Dr. S. M. Akramus Salehin for supervising me. I thank them for their patience, their encouragements and time. I learned a lot from them especially in the area of array signal processing. Specially, Dr. Salehin who taught me how to conduct research and how to write research papers.

Thanks to Professor Andrew Bradley for arranging a visit and seminar at University of Queensland (UQ).

I would like to acknowledge the support from and useful discussions with my fellow research students in the Applied Signal Processing Group. Special thanks to Pei Hua Leong and Farhana Bashar for the constant help on the technical difficulties I faced.

I am indebted to the the administrative staff at the Research School of Information Sciences and Engineering for all their help. Special mention goes to Lesley Goldburg for her assistance in arranging the conference travels undertaken during this Mphil research.

Lastly, I acknowledge the continuous support from my family and my friends during this difficult and stressful time. I am especially grateful to my dad, Jianxin Long, mum Pingya Liao and sister Ying Long for their financial and moral support and my girl friend Wei Zhou for her care in daily life.

Abstract

Recently, adaptive array beamforming has been applied to medical ultrasound imaging and achieved promising performance improvement. However, the current robust Capon beamformer with spatial smoothing (RCB-SS) is implemented in the time domain, which does not fully utilise the large bandwidth of ultrasound signals and spatial smoothing reduces the effective aperture. In this dissertation, we propose a robust Capon beamformer with frequency smoothing (RCB-FS) and compare its performance with RCB-SS. To further reduce the speckle noise and utilise the large bandwidth of the signal, we combine RCB-FS and frequency compounding (FC) and propose a robust Capon beamformer with frequency smoothing combined with frequency compounding (RCB-FS-FC). The proposed RCB-FS method shows a narrower mainlobe width, lower sidelobes, better reconstruction at higher depths and less speckle than RCB-SS. FC is an effective method to improve the contrast resolution and suppress speckle noise by combining sub-band images, at the expense of resolution. Compared to standard FC, the proposed RCB-FS-FC method has a better contrast resolution and speckle reduction and a significant improvement in resolution. RCB-FS offers a promising approach to find the optimal weights for the transducers in forming the sub-band images needed for frequency compounding.

List of Acronyms

DAS	Delay and Sum
CB	Capon Beamformer
RCB	Robust Capon Beamformer
RCB-SS	Robust Capon Beamformer with Spatial Smoothing
RCB-FS	Robust Capon Beamformer with Frequency Smoothing
MVDR	Minimum Variance Distortionless Response
LCMV	Linear Constraint Minimum Variance
ESB	Eigenspace Based
DL	Diagonal Loading
SINR	Signal-to-Interference-Noise Ratio
2D	Two-Dimensional
3D	Three-Dimensional
4D	Four-Dimensional
FWHM	Full Width at Half Maximum
PSL	Peak Sidelobe Level
CNR	Contrast-to-Noise Ratio
SNR	Signal-to-Noise Ratio
HPI	Histogram Pixel Intensity

Notations and Symbols

i	$= \sqrt{-1}$
c	speed of wave propagation
f	frequency
ω	angular frequency equal to $2\pi f$
k	wavenumber equal to $2\pi f/c$
k_l	lower frequency limit
k_h	higher frequency limit
σ^2	noise power
\mathbf{I}	identity matrix
$(\cdot)^*$	complex conjugate operator
$(\cdot)^T$	transpose operator
$(\cdot)^H$	conjugate and transpose operator
$E\{\cdot\}$	expectation operator
$ \cdot $	modulus operator
$\ \cdot\ $	vector norm
$\text{tr}\{\cdot\}$	trace operator

Contents

Declaration	i
Acknowledgements	iii
Abstract	iv
List of Acronyms	v
Notations and Symbols	vi
1 Introduction	1
1.1 Motivation	1
1.2 Medical Ultrasound Imaging	3
1.3 Array Signal Processing	5
1.4 Aims and Scope	7
1.5 Main Contributions	9
1.6 Outline	9
2 Background on Adaptive Array Ultrasound Imaging	11
2.1 Ultrasound Physics	11
2.1.1 Signals	11
2.1.2 Wave Propagation	12
2.2 Adaptive Array Beamformer	22
2.2.1 Capon Beamformer	22
2.2.2 Steering Vector Errors	26
2.2.3 Correlated Signals	28
2.3 Adaptive Beamformer Applied to Ultrasound Imaging	29
2.4 Summary	31
3 Frequency Smoothed Robust Capon Beamformer	32
3.1 Introduction	32

3.2	Problem Formulation	33
3.3	Proposed Beamforming Method	35
3.3.1	Frequency Smoothing	35
3.3.2	Diagonal Loading	39
3.3.3	Computational Complexity	40
3.4	Evaluation Metrics	41
3.5	Wire Targets	41
3.5.1	Overall Image Quality	41
3.5.2	Analysis	42
3.6	<i>Gearbr</i> Phantom	43
3.7	Discussions	43
3.8	Summary	44
4	RCB-FS with Frequency Compounding	51
4.1	Introduction	51
4.2	Speckle Reduction Techniques	53
4.3	Proposed Speckle Reduction Method	54
4.4	Evaluation Metrics	55
4.5	RCB-FS with Long Observation Time	58
4.5.1	Wire Targets	58
4.5.2	Phantoms	60
4.6	RCB-FS-FC	60
4.6.1	Overall Image Quality	60
4.6.2	Analysis	62
4.7	Discussions	65
4.8	Summary	68
5	Conclusions and Future Work	69
5.1	Conclusions	69
5.2	Future Work	70
	Bibliography	72

List of Figures

1.1	A reflection tomography system.	3
1.2	Block diagram showing the components in reflection tomography.	4
1.3	The beampattern of DAS with signal of interest coming at $-\pi/6$ and interference impinging from $\pi/6$	5
1.4	The beampattern of DAS weighted by a Hanning window with signal of interest coming at $-\pi/6$ and interference impinging from $\pi/6$	6
2.1	The reflectivity distribution of five point reflectors at distances 10mm, 16mm, 24mm, 33mm, 40mm and 43mm.	15
2.2	The received signals from five point reflectors at distances 10mm, 16mm, 24mm, 33mm, 40mm and 43mm.	15
2.3	The coordinate system used in medical ultrasound system.	19
2.4	The illustration of the propagation of focused beam.	20
2.5	The illustration of an array system with farfield signal source and interference.	22
2.6	Beam Pattern of Capon beamformer with uncorrelated signals: signal from 0 radians and interference from $\pi/8$ and $\pi/6$ radians.	25
2.7	Beam Pattern of Capon beamformer with correlated signals: signal from 0 radians and interference from $\pi/8$ and $\pi/6$ radians.	26
3.1	The block diagram of RCB-FS.	37
3.2	The beam pattern of Capon beamformer with spatial smoothing: signal from 0 radians and interference from $\pi/8$ and $\pi/6$ radians.	45
3.3	The beam pattern of Capon beamformer with frequency smoothing: signal from 0 radians and interference from $\pi/8$ and $\pi/6$ radians.	45
3.4	The beam pattern of robust Capon beamformer with frequency smoothing and diagonal loading: signal from 0 radians and interference from $\pi/8$ and $\pi/6$ radians.	46
3.5	Illustration of FWHM and PSL.	46

3.6	Images obtained from experimental data of wire targets: (a) DAS, (b) RCB-SS and (c) RCB-FS-short using the full aperture. Images obtained from (d) DAS, (e) RCB-SS and (f) RCB-FS-short using only half the aperture.	47
3.7	Lateral variation of wire targets using the full aperture at depths of (a) 48 mm and (b) 83 mm.	48
3.8	Axial variation of wire targets using half the aperture at the 74th scanline (52°) with (a) DAS, (b) RCB-SS and (c) RCB-FS-short. . .	49
3.9	Images obtained from experimental data of a <i>Gearb</i> phantom with 64 sensors using (a) RCB-SS and (b) RCB-FS-short.	50
4.1	Block diagram of RCB-FS-FC.	52
4.2	The illustration of interference from two point reflectors.	53
4.3	Images obtained from experimental data of wire targets: left: (a) DAS, (c) RCB-SS and (e) RCB-FS-short, (g) RCB-FS-long using full aperture; right: (b) DAS, (d) RCB-SS, (f) RCB-FS-short and (h) RCB-FS-long using half aperture.	57
4.4	Axial variation of wire targets using half the aperture at the 74th scanline (52°) with (a) DAS, (b) RCB-SS, (c) RCB-FS-short and (d) RCB-FS-long.	59
4.5	Images obtained from heart phantoms: using (a) RCB-SS, (c) RCB-FS-short and (e) RCB-FS-long and <i>gearb</i> phantoms: using (b) RCB-SS, (d) RCB-FS-short and (f) RCB-FS-long.	61
4.6	Edge detection of lesion in <i>gearb</i> phantoms using: (a) RCB-SS and (b) RCB-FS.	62
4.7	Compounded B-mode Images: obtained from <i>gearb</i> phantom using: (a) FC with half bandwidth, (b) RCB-FS-FC with half bandwidth, (c) FC with one-fourth bandwidth, (d) RCB-FS-FC with one-fourth bandwidth, (e) FC with one-eighth bandwidth and (f) RCB-FS-FC with one-eighth bandwidth.	63
4.8	Sub-band B-mode Images: obtained from <i>gearb</i> phantom using: (a) FC with one-fourth bandwidth and (b) RCB-FS-FC with one-fourth bandwidth.	64
4.9	Histogram for <i>gearb</i> phantom: (a) FC with half-width, (b) RCB-FS-FC with half-width, (c) FC with fourth-width, (d) RCB-FS-FC with fourth-width, (e) FC with eighth-width and (f) RCB-FS-FC with eighth-width.	66

4.10 Edge detection of lesion (bright circle region) in <i>geabr</i> phantom: (a) FC with half-width, (b) RCB-FS-FC with half-width, (c) FC with fourth-width, (d) RCB-FS-FC with fourth-width, (e) FC with eighth-width and (f) RCB-FS-FC with eighth-width.	67
--	----

List of Tables

1.1	Comparison of medical imaging modalities [1].	2
3.1	Average FWHM and PSL of different algorithms using full aperture	42
4.1	Average FWHM and PSL of different algorithms	58
4.2	Speckle Statistics	65

Chapter 1

Introduction

1.1 Motivation

Medical ultrasound imaging is a soft tissue imaging modality with a wide range of clinical applications including cardiology, urology, obstetrics and gynaecology, general abdominal and vascular imaging and guide in surgical procedures [2]. Medical ultrasound imaging is widely used due to its:

- **High temporal resolution** - Provides real time imaging since the duration of time for producing an image is very fast.
- **High safety** - The imaging process is non-invasive and non-ionising.
- **Easy manipulation** - The transducer can be operated manually and the size of transducer is small allowing signals to be transmitted between ribs or other obstructions.
- **Low cost** - The cost of imaging is very low and the ultrasound system is not as expensive as the other medical imaging systems such as computed tomography (CT) or magnetic resonance imaging (MRI).

In Table 1.1, a comparison between medical ultrasound system and two other widely used medical imaging systems, namely, MRI and CT is given [1]. We can see that one of the main drawbacks of medical ultrasound imaging is the low **penetration**¹. Penetration is dependent on the frequency of the ultrasound wave and the acoustic impedance² of the medium. A 4 MegaHertz (MHz) ultrasound penetrates up to

¹Penetration is a measure of how deep the ultrasound wave can penetrate into a material. In ultrasound imaging, we define penetration as axial direction

²Acoustic impedance is defined as the resistance of the particles of the medium to mechanical vibrations.

Properties \ Equipment	Ultrasound	MRI	CT
Expense	cheapest	most expensive	expensive
Scan time	real-time	10-45 mins	very long
Ionising	no	no	yes
Contrast Agents	no	yes (with good safety)	yes
Imaging direction	any	any	axial only
Image Quality	not detailed	best	good
Penetration	low	high	high

Table 1.1: Comparison of medical imaging modalities [1].

about 40 mm in fat while only about 10 mm in muscle. In contrast, a 1 MHz ultrasound pulse penetrates four times as far as a 4 MHz wave - penetration increases when frequency decreases. Also, the penetration of ultrasound waves in bone is almost nil [3].

Another drawback of ultrasound imaging system is the low image quality. The main measures of image quality for an ultrasound system include:

- **Spatial resolution** - the minimum distance that two things can be visibly resolved from each other. In ultrasound imaging, the spatial resolution we usually focus on is the direction perpendicular to the penetration, which we call it lateral direction.
- **Contrast resolution** - the ability to distinguish two different intensities in the image.
- **Artefact** - any structure in the image that does not correlate directly with the actual tissue [4, page 179].

Like penetration, spatial resolution is frequency dependent but now when frequency decreases, the spatial resolution decreases. In clinical ultrasound whose frequency range is around 1 - 10 MHz, the penetration can go up to 100 mm, but the resolution is only around 1 mm. In micro-ultrasound where the frequency used is higher than 30 MHz, the resolution can go down to the micrometer range (20 - 100 μm), but the penetration is less than 10 mm [5]. Besides spatial resolution, contrast resolution can be improved and the artefacts can be reduced by trading some properties of the ultrasound system like penetration and temporal resolution. Therefore, a significant research challenge in ultrasound imaging is to produce images with good image quality, high penetration and high temporal resolution.

A widely used approach to improve image quality is array signal processing. It is a technique using a group of transducers to extract both the **spatial** and **temporal** information from the environment. The key applications are: radar,

sonar, communications, imaging, geophysics, astronomy and biomedicine [6, page 201], where spatial or directional information is important. In medical ultrasound imaging, the array signal processing techniques have to cope with some practical situations like **broadband signals** (signals with a non-negligible fractional bandwidth, computed as the ratio of the signal bandwidth to the centre frequency of the signal), multi-path **correlated signals** (signals from one source but with two or more paths and therefore, they are similar) and some other restrictions such as transducer size and number due to clinical manipulability. In recent years, many researchers are working on how to implement the array signal processing techniques onto medical ultrasound imaging system and improve its performance including spatial resolution, temporal resolution and contrast resolution [7–14]. In this dissertation, we are going to review the array signal processing techniques applied to medical ultrasound imaging and propose a new array signal processing approach to improve the image quality of medical ultrasound images.

1.2 Medical Ultrasound Imaging

Reflection tomography, a quantitative cross sectional image reconstructed from reflection data [15, Page 297], is typically used to construct medical ultrasound images because the penetration of ultrasound wave is relatively weak to go through human body for transmission tomography. A simple reflection tomography system is illustrated in Figure 1.1. An array of transducers sends out signals to the area

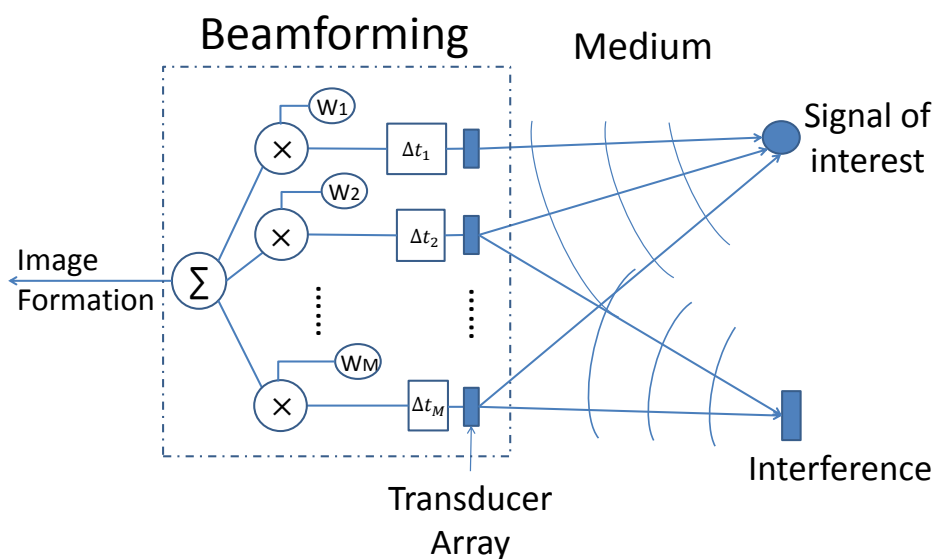


Figure 1.1: A reflection tomography system.

of interest and this same array is used to receive the reflected signals from a target. One advantage of reflection tomography is that transmission and reception are done by the same transducer array and it is not necessary to receive the data by encircling the target with many receivers as in transmission tomography. However, as the array is not mono-directional, which is usually the case in ultrasound imaging, the received signals contain both the signal of interest and interference. It is hard to separate the interference in reflection tomography due to the lack of spatial information. An array signal processing step, or beamforming, can effectively extract the spatial information and suppress the interference and hence, it is a significant step before forming the image.

We can summarise the reflection tomography system by the following four steps:

1. transmission, 2. wave propagation, 3. reception and 4. image formation, as shown by the block diagram in Figure 1.2.

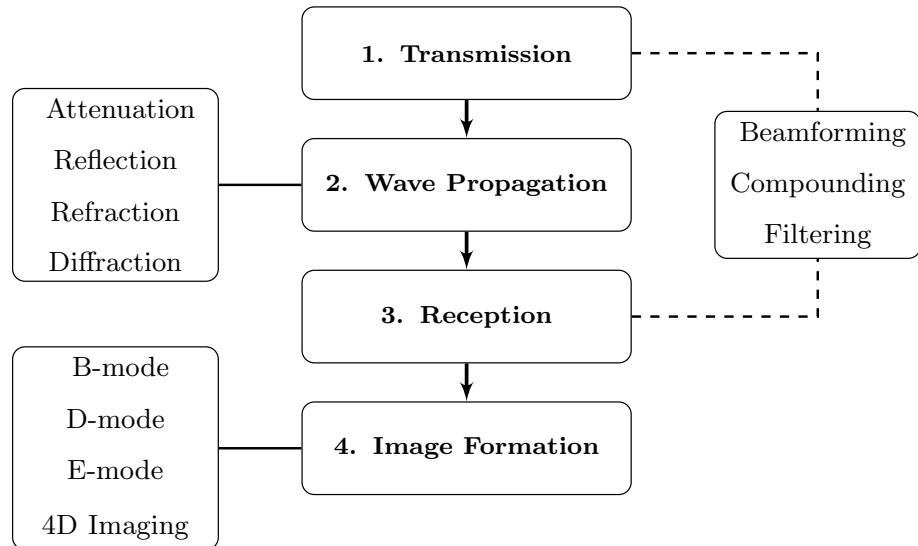


Figure 1.2: Block diagram showing the components in reflection tomography.

A detailed description of an ultrasound system is provided in Chapter 2. We will cover the transmit-receive techniques such as beamforming and compounding. Moreover, we will discuss the way ultrasound waves propagate and interact with the medium, including attenuation, reflection, refraction and diffraction. Furthermore, we will introduce some typical image formation modes like B-mode, D-mode, E-mode and 4D imaging.

1.3 Array Signal Processing

Array processing uses a spatial filter to filter out the signals from regions (directions) out of interest. From the beamforming part in Figure 1.1, assuming that we have known the direction of the interested signal, delays Δt can be found for each transducer according to the direction of the signal of interest so that the waveform coming from the signal of interest sums in phase³. By summing the signals with different delays, the signals of interest is undistorted while the signals out of phase are suppressed. This is called a Delay-and-Sum (DAS) beamformer, which is the simplest but essential realisation of an array signal processing system. The output, or beampattern⁴ of a DAS beamformer is simulated and shown in Figure 1.3

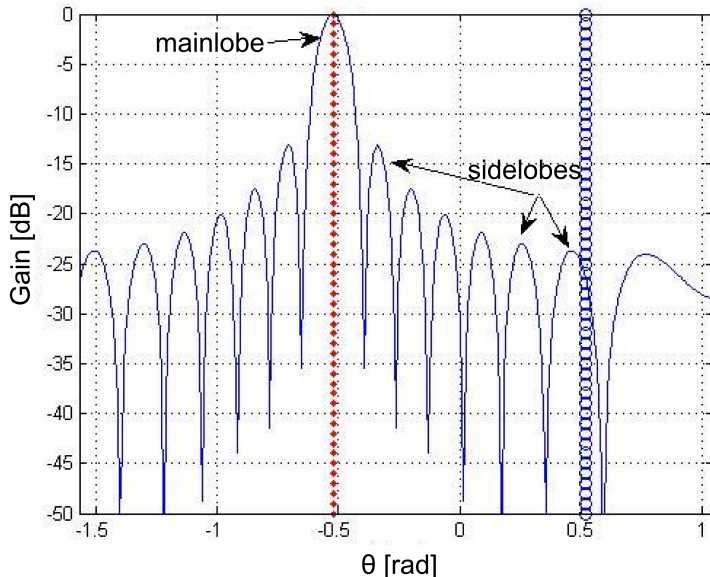


Figure 1.3: The beampattern of DAS with signal of interest coming at $-\pi/6$ and interference impinging from $\pi/6$.

Here, the signal of interest is coming from $-\pi/6$ radian and the interference is from $\pi/6$ radian. The number of transducers is 16. Delays, or steering vector⁵ is applied to each transducer to focus at $-\pi/6$, $[e^{i\theta}, e^{i2\pi\frac{d}{\lambda}\sin\theta}, \dots, e^{i2\pi(M-1)\frac{d}{\lambda}\sin\theta}]$, where θ is $-\pi/6$, d is the distance between sensors and λ is the wavelength of the signal.

From Figure 1.3, the signals from the direction of interest are maintained, while the signals from other directions are suppressed. However, the beam pattern of a

³Phase in sinusoidal functions or in waves is defined as the fraction of the wave cycle which has elapsed relative to the origin [16, pages,1499]. In phase means two waves have the same frequency and no phase difference.

⁴Beampattern refers to the directional dependence of the power of the waves at the array [17]

⁵Steering vector is a sequence of phasors whose exponents are chosen to cancel the plane-wave signal's propagation-related phase shift [18]

DAS beamformer does not only consist of the local maxima from the direction of interest, but also from some other directions. The local maxima from the direction of interest is called mainlobe, while the ones from other directions are called sidelobes. The interferences from sidelobes are not suppressed properly and they corrupt the reception of the signal of interest. One way of suppressing the sidelobe interference is by applying apodisations⁶, or weights to each sensor. Some typical weights are like Hanning, Hamming and Blackman window. These weights are data independent, which suppress all the side-lobes while widening the mainlobe width as shown on Figure 1.4. When the mainlobe is widened, a wider sector of signals will be maintained and cannot be distinguished, which lowers the resolution. Again, the number of transducers is 16. The signal of interest is from $-\pi/6$

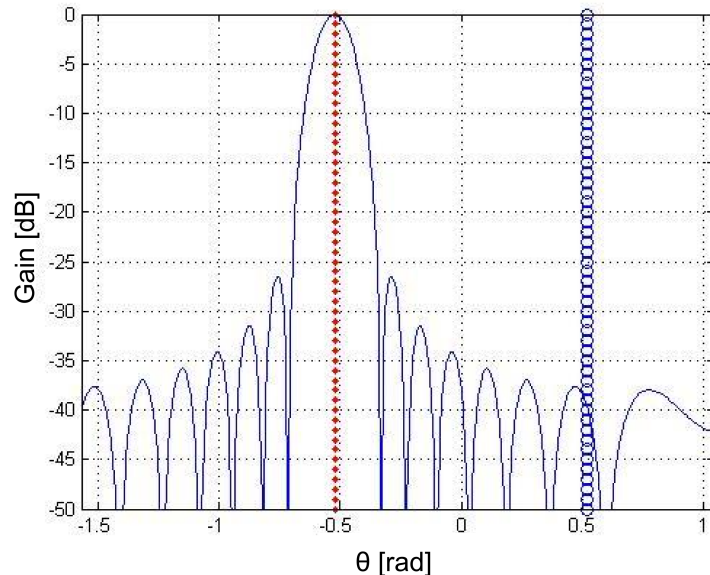


Figure 1.4: The beampattern of DAS weighted by a Hanning window with signal of interest coming at $-\pi/6$ and interference impinging from $\pi/6$.

radian and the interference is from $\pi/6$ radian. Hanning weights are applied to each delayed signal.

Compared to data-independent weights, data-dependent or adaptive weights can achieve both a high resolution and good interference suppression because the suppression or nullings are only applied to directions the interference comes from, instead of suppressing all the sidelobes. Finding weights adaptively based on the data statistics is called adaptive beamforming. A commonly used adaptive beamformer is Capon beamformer, which is the beamformer mainly discussed in this dissertation. In Chapter 2, a detailed discussion on the Capon beamformer [20]

⁶Apodisations are used to decrease the amplitudes of the sidelobes at the cost of increasing the mainlobe [19].

and its robustness against certain practical situations like correlated signal and steering vector errors will be given.

1.4 Aims and Scope

From the above discussion we know that medical ultrasound is a widely used biomedical imaging modality that provides excellent temporal resolution images with low cost and high safety. However, these images suffer from low spatial resolution and high background noise. Hence, many methods have been proposed to improve the image quality without losing the temporal resolution. Among these methods, array beamforming is one of the most significant ones. Delay-and-sum (DAS) is a typically used beamforming method in clinical ultrasound. DAS applies delays and data-independent apodisations on every single transducer to extract information about a signal originating from a particular point. Compared to DAS, by adapting the apodisations to the data, adaptive Capon beamforming can achieve a better lateral resolution and off-axis interference suppression, provided that the steering vector is precisely known. Moreover, the Capon beamformer was implemented on a GPU for practical use [21]. To reduce steering vector errors, different robust methods were implemented on the Capon beamformer to achieve a better performance. Recently, robust Capon beamformers (RCB) including linear constraint minimum variance (LCMV) [7], generalized sidelobe canceller (GSC) [9], diagonal loading (DL) [10] and eigenspace-based methods [13] have been applied to ultrasound imaging and achieved some significant improvement on image quality. This motivates us to study and develop a better RCB algorithm to further improve the image quality.

In ultrasound imaging, an active array system is used. However, the coherency of the signals deteriorates the performance of RCB. Recently, a decorrelation method proposed by Wang et al. decorrelates the signals by averaging the spatial covariance matrix over different single transmissions from different directions [22]. However, these single transmissions suffer from low singal-to-noise ratio (SNR) and a focused beam is typically transmitted in clinical ultrasound. Compared to single transmissions, sub-aperture forward-only spatial smoothing [8–14] and forward-backward smoothing [23] methods have been used to decorrelate the signals. However, sub-aperture spatial smoothing cannot reduce the coherence if the coherent sources are closely spaced [24] and the lateral resolution is reduced due to a reduction in the effective aperture. Since broadband signals are used in ultrasound imaging, it is superior to suppress the interference by the phase differences

in the different frequencies. However, all of the aforementioned RCB methods are implemented in the time domain. Holfort et al. investigated a frequency domain sub-band beamforming method [14]. The performance of this sub-band beamforming is limited by the low SNR of the single sub-bands and a sub-aperture spatial smoothing process is still needed to decorrelate the signals.

In this dissertation, we propose a robust Capon beamformer with frequency smoothing (RCB-FS) for ultrasound imaging. This RCB-FS is an adaptive beamforming method implemented in the frequency domain, which can fully utilize the whole bandwidth of the received signals. Frequency smoothing is used instead of sub-aperture spatial smoothing, which does not reduce the effective aperture and is able to decorrelate even closely located scatterers. To the best of our knowledge, this is the first time a frequency domain RCB with Frequency Smoothing (RCB-FS) has been proposed for ultrasound imaging. We evaluate our method using full width at half maximum (FWHM) and peak side-lobe (PSL) and compare to the DAS and RCB-SS beamforming methods.

In order to further reduce the speckle noise, we propose a new algorithm combining RCB-FS and frequency compounding (FC) as a further frequency domain implementation. FC is one of the most commonly used speckle-reduction techniques. The speckle pattern in ultrasound images comes from the interference due to sub-resolution scatterers, and this interference differs in different frequencies. FC combines these different frequency images to reduce speckle [25]. In this dissertation, the different frequency images are obtained by dividing the spectrum of the original received data into sub-bands and forming different images from the different sub-bands. This method is also called split spectrum processing [26–28]. The main disadvantage of this method is the deterioration of the axial resolution. However, in our proposed RCB-FS-FC method, high resolution apodisations are found for all the sub-band images. RCB-FS-FC offers a new idea for finding the optimal weights for transducers to obtain sub-band images. In this dissertation, we compare our RCB-FS-FC method to standard FC method and evaluate the image quality by contrast-to-noise Ratio (CNR), speckle signal-to-noise ratio (sSNR), histogram pixel intensity (HPI) and margin strength (MS) methods.

We answer the following questions in this thesis:

- How can we utilise the broad bandwidth in ultrasound imaging to improve the performance of the adaptive beamformer?
- Can we design a frequency domain adaptive beamformer that can perform image reconstruction for multipath propagation with correlated interferences?

- How can we decorrelate the ultrasound signals without a loss in the effective aperture?
- What aspects of performance can this adaptive beamformer improve for medical ultrasound imaging?
- With further extension, can our broadband adaptive beamformer lead to better speckle reduction in the ultrasound images?

1.5 Main Contributions

The main contributions of this dissertation are provided below:

- We proposed a new adaptive beamforming method applied to ultrasound imaging. This is the first time a frequency domain RCB with Frequency Smoothing (RCB-FS) has been proposed for ultrasound imaging. We further combine the RCB-FS method with frequency compounding (FC) and propose a RCB-FS-FC method to reduce speckle noise in the reconstructed images.
- The proposed methods have been investigated on real ultrasound signals. We investigated the performance of RCB-FS and found that our method has a narrower mainlobe width, lower sidelobes, stronger interference suppression, less speckle and better reconstruction at higher depths than RCB-SS and DAS beamforming. The proposed method also shows better performance when the aperture size is reduced, thus allowing higher frame rates and lower data storage.
- We showed that compared to standard FC, the proposed RCB-FS-FC method has a better performance in speckle reduction and a significant improvement in resolution. RCB-FS offers a promising way to find the optimal weights for the transducers in forming the sub-band images needed for frequency compounding.

1.6 Outline

This section outlines the structure and main contributions of this dissertation.

This thesis is organized as follows:

- Chapter 2 provides some background knowledge on medical ultrasound imaging system and adaptive array beamforming. Latest research progress in these

two areas is also included. In addition, a review of adaptive beamforming applied to medical ultrasound imaging is highlighted.

- Chapter 3 demonstrates the performance of the proposed RCB-FS method to improve image quality, especially spatial resolution for ultrasound imaging. A proof of the proposed method to suppress correlated interference. We also provide experimental results of the proposed RCB-FS method applied to wire targets and a *gearbr* phantom from the Biomedical Ultrasonics Laboratory, University of Michigan at Ann Arbor [29]. The result from our proposed method are compared with results from the DAS and the RCB-SS method.
- Chapter 4 extends the RCB-FS method and investigates the RCB-FS-FC method. We also provide a brief summary of different despeckling techniques. The proposed RCB-FS-FC is applied to a heart phantom and *gearbr* phantom [29] and its performance compared with the standard FC method.
- Chapter 5 concludes the dissertation and provides a discussion on future works related to the research in this thesis.

Chapter 2

Background on Adaptive Array Ultrasound Imaging

After an overview of the motivations, aims, contributions and structure of the dissertation given in Chapter 1, this chapter provides the necessary background knowledge and literature review for this thesis. Firstly, we provide a background of the physics of an ultrasound system including the type of signals used and the way these signals propagate and interact with the medium. Latest progress of researches on ultrasound imaging are introduced and the relationship to the proposed method in this dissertation is given. Chapter 2.2 looks at the minimum variance Capon beamforming and its enhancement against correlated signals and robustness to steering vector errors. The last section focuses on adaptive array beamforming applied to medical ultrasound imaging and reviews the recent research progress in this area.

2.1 Ultrasound Physics

2.1.1 Signals

In medical ultrasound imaging, 1-20 MegaHertz (MHz) acoustic wave is typically used [4]. As mentioned in the introduction, the choice of frequency is a trade-off between resolution and penetration. In some applications like brain imaging, a high frequency acoustic pulse is used to provide a good resolution while in some deeper areas like kidney and liver, low frequency waves are manually used. The bandwidth of the ultrasound transducer is usually wide, which has a fractional bandwidth of about 30-50%. A wide bandwidth signal is short in time domain and

it can be modeled as an amplitude modulated sinusoid, [30],

$$s(t) = a(t)e^{-i2\pi f_0 t}, \quad (2.1)$$

where $a(t)$ is the envelop function which is a short pulse in time domain and f_0 denotes the carrier frequency. The pulse shape determines the penetration, frame rate and the signal-to-noise-ratio (SNR) and signal distortion, which influence the image quality. However, each pulse shape will only do well in some properties instead of all. Choosing a proper pulse shape is an important factor in ultrasound imaging. Pulse compression is a special approach using coded pulses with longer duration and lower amplitude compared to a short pulse. Pulse compression can increase the SNR with good penetration and frame rate by selecting an appropriate coding [31, 32]. Coded excitation is also applied to ultrasound imaging for specific enhancement like speckle reduction [27, 28]. In this dissertation, the typical short pulse is considered; anyone interested in the pulse compression can combine the proposed beamforming methods with coding pulses to study a better image reconstruction. In the later discussion, we assume that the pulse shape of the signal is optimised and $s(t)$ will be used to describe the transmitted signal.

2.1.2 Wave Propagation

After knowing the signals transmitted into the medium, we are going to discuss the way these signals propagate in the medium. The ultrasound wave belongs to the class of mechanical waves, and therefore, along with the propagation of ultrasound wave, the particle in the medium will react with the wave and vibrate, which will generate harmonic waves. The use of harmonic waves to generate image is called harmonic imaging, which can achieve a higher resolution, better contrast and less artefact [33, 34], because the signals are generated along with the propagation instead of attenuating along with the propagation. In this dissertation, the harmonic imaging method is not applied; future work includes combining the harmonic imaging with our adaptive array beamforming method to further improve the image reconstruction. In this dissertation, as harmonic imaging is not considered, we assume particle vibrations are small and hence a linear wave equation can be used to describe the propagation of the ultrasound wave.

If $p(x, y, z, t)$ denotes the acoustic pressure at point (x, y, z) at time t , the linear wave equation can be written as,

$$\nabla^2 p = \frac{\partial^2 p}{\partial x^2} + \frac{\partial^2 p}{\partial y^2} + \frac{\partial^2 p}{\partial z^2} = \frac{1}{c} \frac{\partial^2 p}{\partial t^2}. \quad (2.2)$$

where c is the speed of ultrasound wave in the medium. Here, we note that under the linear approximation, the propagation mechanism of ultrasound waves is the same as the electromagnetic waves and therefore, some concepts in optics can be used here:

- **Free-space wave propagation:** Assuming there is no interaction between the ultrasound wave and the medium, the ultrasound wave of a specific frequency f at position \mathbf{r} sent out from the origin can be described as,

$$p_f(\mathbf{r}, t) = p_f(0, 0)e^{i2\pi f(t-\mathbf{r}/c)}, \quad (2.3)$$

This is a specific class of solutions to the wave equation. From this solution, we can see that in free space, the wave will keep its initial properties along propagation. We can rewrite the free-space wave propagation using the signal transmitted as,

$$p_f(\mathbf{r}, t) = s_f(t - \mathbf{r}/c), \quad (2.4)$$

where $s_f(t) = a(t)e^{-i2\pi ft}$ as defined in (2.1).

- **Attenuation:** In practice, interactions are inevitable for the ultrasound wave. Along with the propagation, ultrasound waves attenuate due to scattering and absorption [4]. Attenuation can be described as an exponential frequency and distance dependent factor as follow,

$$p_f(\mathbf{r}, t) = p_f(0, 0)e^{-\alpha(f)||\mathbf{r}||}; \quad (2.5)$$

where $||\cdot||$ denotes the Euclidean norm of a vector and $\alpha(f)$ is the attenuation coefficient, which is dependent on the medium and the frequency of the ultrasound wave. The higher the frequency, the larger the attenuation coefficient becomes. Hence, high frequency ultrasound waves have low penetration as mentioned in Chapter 1. The propagation of ultrasound wave in a uniformly distributed medium is,

$$p_f(\mathbf{r}, t) = e^{-\alpha(f)||\mathbf{r}||}s_f(t - \mathbf{r}/c). \quad (2.6)$$

The attenuation of ultrasound wave can be easily compensated by a time gain compensation (TGC) factor $e^{\alpha(f)ct}$ [4], where $ct/2 = \mathbf{r}$ after a round-trip in a reflective system. In later discussion, we assume that attenuation has been compensated by TGC.

- **Reflection:**

Reflection is one of the most important interactions between ultrasound wave and the medium. Two important types of reflections are surface reflections and volumetric scattering [4].

Surface reflections happen when the wave is directed to a smooth interface where the refractive index changes. Some energy of the wave will be reflected back to a specific direction according to Fresnel equations¹. We define the pressure reflectivity at interface z as,

$$R(z) = \frac{p_{ref}}{p_{in}}, \quad (2.7)$$

where p_{ref} is the acoustic pressure of the reflected wave and p_{in} is the acoustic pressure of the incoming wave before reflection. In reflective mode ultrasound imaging, the reflectivity will be recorded and used to reconstruct images. Assuming in a one dimension case, there are interfaces with reflectivity $R(z_1), \dots, R(z_N)$ at depths z_1, \dots, z_N ,

$$R(z) = \sum_{n=1}^N R(z_n) \delta(z - z_n), \quad (2.8)$$

where δ is the Dirac delta function. Then, the received signal from the transducer is,

$$p_f(t) = R_0 \sum_{n=1}^N R(z_n) s_f \left(t - \frac{2z_n}{c} \right), \quad (2.9)$$

where R_0 is a gain factor.

In ultrasound imaging, our task is to use the received signal shown in Figure. 2.2 to estimate the reflectivity shown in Figure. 2.1, and then reconstruct the image to diagnose the situations of different soft tissues in the area of interest.

Apparently, even in this simplified model, the received signal is not equal to the reflectivity, as the received signal is blurred out by the length of pulse $s_f(t)$. As a result, the resolution ζ in this model is limited by the length of pulse,

$$\zeta = \text{length}\{s_f(t)\}. \quad (2.10)$$

From the expression above, in order to improve the resolution, a short pulse

¹Fresnel equation gives the reflection and transmission coefficients for waves parallel and perpendicular to the plane of incidence [35]

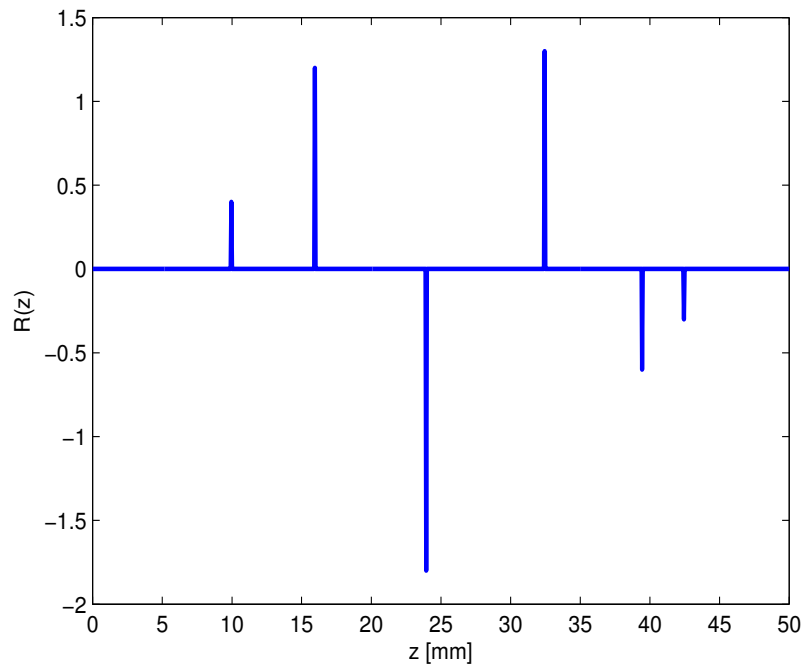


Figure 2.1: The reflectivity distribution of five point reflectors at distances 10mm, 16mm, 24mm, 33mm, 40mm and 43mm.

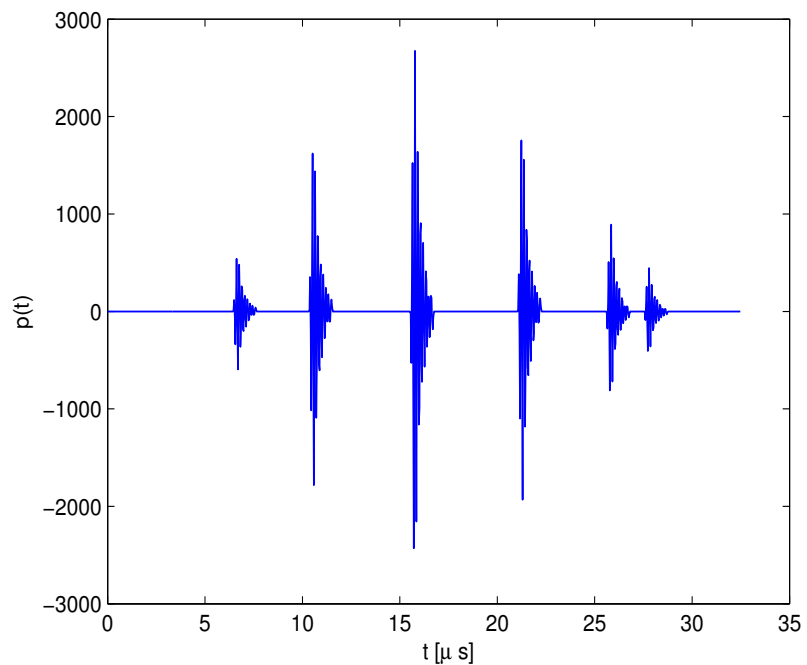


Figure 2.2: The received signals from five point reflectors at distances 10mm, 16mm, 24mm, 33mm, 40mm and 43mm.

is used (or a coded signal, but this is not discussed in this dissertation). However, a short pulse has a wide bandwidth. As the attenuation is frequency dependent, different frequency components will attenuate differently along with propagation and result in distortion. This distortion is called dispersion. Dispersion can be minimised by using Gaussian pulse envelopes [36]. Therefore, in this dissertation we use pulse $s_f(t)$ that have gaussian envelopes and the dispersion is assumed to be 0 and in later discussions, $s(t)$ will be used instead of $s_f(t)$ for simplification.

Medical ultrasound imaging utilise the specular reflection of different soft tissues. However, some specular reflections will result in artefacts like reverberation, shadowing and multi-path reflections, which deteriorate the reconstructed images:

- *Reverberation* comes from multiple reflections from two closely spaced interfaces. In the reconstructed image, these additional reflections will be recorded and cause artefacts. The *reverberation artefact* in ultrasound imaging is created by the layer with a large reflectivity perpendicular to the propagation direction [37]; strong reflections will be created and recorded as multiple parallel interfaces. Reverberation can also be created by two strong reflectors; in the case of small reflectors, a *comet tail phenomenon* can be observed in the reconstructed image. A closely related phenomenon is the *ring-down artefact*, which comes from the resonance of a small gas bubble. In this case, reflections will be sent out constantly. Some researchers are working on reverberation reduction using filters [38].
- *Shadowing artefact* is the signal reduction due to a strong reflector during propagation [39]. The area imaged after the wave passes through the strong reflectors will be dark and shadowed. These strong reflectors usually occur at the boundaries of tissue and bone, or tissue and gas.
- Multi-path reflections occur when the signal is reflected back from an undesired path - non-perpendicularly reflected [40]. This signal will be reconstructed and put onto the wrong place and become an artefact. *Mirror image artefact* is an example of multi-path reflections. In the reconstructed image with mirror image artefact, a visual object is reconstructed symmetric to the real object with respect to the reflective interface.

Another type of reflection is volumetric scattering, or diffuse reflection where

the incoming wave will be reflected to a broad range of angles. Scattering comes from the reflections from sub-wavelength particles. When the particles are much smaller than the wavelength, Rayleigh scattering will occur. This scattering has a strong frequency dependence (f^2 to f^6). In addition, due to the interference, or superposition of waves from the small reflectors, *speckle artefacts* occur. If waves with the same frequency are in phase, they will be enhanced while waves out of phase will be reduced and even cancelled. For imaging purposes, speckle artefacts will influence the observation of details in the image and many researches are working on minimizing it [41]. In Chapter 4, further discussions on speckle reduction techniques including frequency compounding, spatial compounding and post filtering will be given. In this dissertation, we combine our proposed beamforming with frequency compounding - an effective speckle reduction technique at the expense of resolution - to reduce the speckle noise with a good spatial resolution. Apart from speckle reduction, as the speckle is highly frequency dependent, speckles can be used to characterise different tissues [42].

- **Refraction:**

Refraction is the bending of ray propagation when the wave strikes the interface of a reflector at an angle other than 90° . This bending will lead to artefact like *mis-registration* in the reconstructed image. The mis-registration causes improper placement, and size and shape distortion in the image. In addition to mis-registration, as a focusing beam is usually used in ultrasound imaging, the refraction results in a *defocusing effect*. However, according to Snell's law, this refraction effect is dependent on the change of wave velocity; for medical ultrasound, the velocity remains approximate constant, around 1540 mm/ms in biological tissue. Therefore, refraction is not a major problem in medical ultrasound imaging and in this dissertation, refraction is ignored.

- **Diffraction:**

In the discussion before, we have come up with the wave propagation model in free-space and in medium with attenuation and reflection. However, in practice, when the wave is sent out from the transducer on the order of wavelength, it will diverge due to diffraction. The divergence of the wave is determined by the transducer field pattern, or point spread function $\xi(x, y)$. In this case, we can re-write the wave propagation model as,

$$p(t) = R_0 \int \int \int R(x, y, z) \xi(x, y) s \left(t - \frac{2z}{c} \right) dx dy dz. \quad (2.11)$$

$p(t)$ is the received signals of medical ultrasound imaging. In typical medical ultrasound imaging, $\xi(x, y)$ is assumed to be independent of z , the axial direction. Using scanlines of data, we can form the following images:

- **A-Mode:** For each transmission, a scanline of signals are received and used to reconstruct an image. This image formation is called A-mode imaging. A-mode imaging can be used in echoencephalography and tissue characterization [4, page 85].
- **B-Mode:** By combining multiple scanlines along with x , lateral direction, a B-mode image is reconstructed. This is the most widely used medical ultrasound image formation. In this dissertation, the proposed methods are mainly applied to this image formation.
- **D-mode:** Doppler mode, D-mode imaging, is utilising the Doppler effect² to image the moving direction of targets. D-mode imaging is a valuable diagnostic method for many vascular pathologies [43]. In D-mode imaging, the temporal resolution is the most important factor.
- **E-mode:** Elasticity mode, E-mode imaging is utilising the relationship between the mechanical wave and elasticity to diagnose the elasticity of the tissue. The E-mode image is usually generated by the radio-frequency signals from an ultrasound scanner, but recent researches investigate the feasibility of elasticity estimation directly from a B-mode image using segmentation and shape analysis [44], which enables the combination with the proposed beamforming method in this dissertation.
- **Tissue harmonic imaging:** Tissue harmonic imaging is a new and significant research topic in ultrasound imaging [45]. The concept of harmonic imaging was discussed before. The typical way to obtain a harmonic image is by using pulse inversion technique: cancelling the fundamental wave by adding the signals received from transmitting the pulse followed by its inverted replica.
- **4D Imaging:** 3D or 4D ultrasound imaging is another most recent research topic. The 4D ultrasound imaging can reconstruct the three dimension structure in real time. Applying Capon beamforming methods to this new image formation is an important direction of researches and has attracted researchers' attentions [46].

²Doppler effect represents the frequency change of a wave due to the movement of the sender or of the receiver

From (2.11), we note that the reflectivity R is blurred out by both $\xi(x, y)$ and $s(t)$. In ultrasound imaging, we call the x, y, z as the lateral, elevational and axial direction as shown in Figure 2.3. The two axis that determine

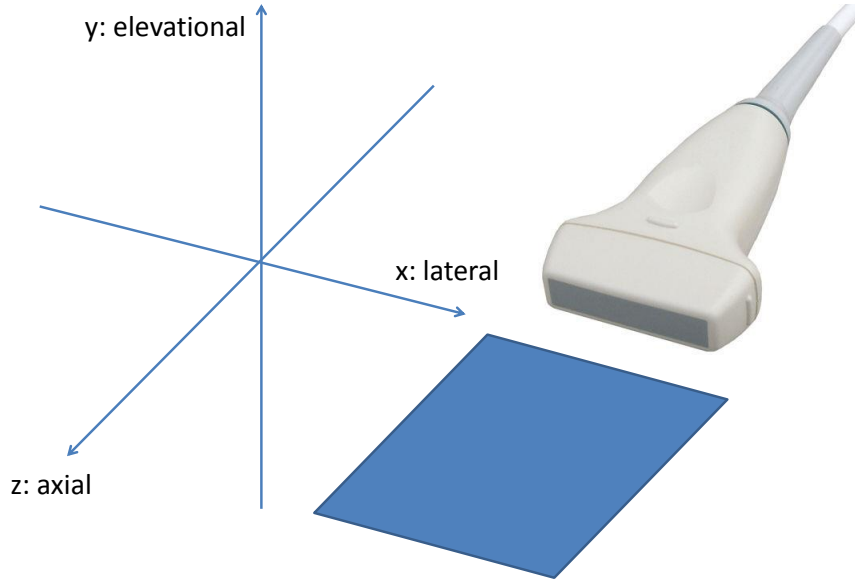


Figure 2.3: The coordinate system used in medical ultrasound system.

the resolution of the reconstructed image are lateral resolution and axial resolution. From (2.11), it is not hard to see that these two resolutions are determined by,

$$\zeta_{lateral} = \text{length}\{\xi(x)\} \quad (2.12)$$

$$\zeta_{axial} = \text{length}\{s(t)\} \quad (2.13)$$

Here, the $\text{length}\{\xi(x)\}$ denotes only the main lobe of the signal. As discussed before, the length of pulse $s(t)$ is minimized by using a pulse with large bandwidth. However, in practice, $\xi(x)$ is changed along with the axial direction, or depth. In Figure 2.4, the change of $\xi(x)$ of a focused beam is shown. In a focused beam, $\xi(x)$ is minimized at the focal point but $\xi(x)$ is large at both nearfield and farfield, which means a low lateral resolution. In addition, for focused beam, the larger the aperture size is, the smaller $\xi(x)$ at the focal point can be, but the more curved the beam will be. A curved beam will create distortions in the image.

Since the lateral resolution is changing along with the depth, how to obtain an image with a good lateral resolution at all depth becomes a significant

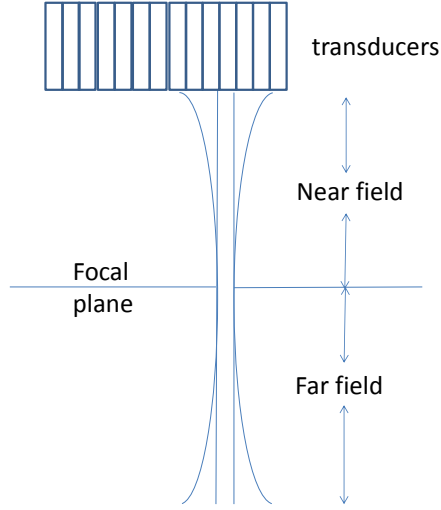


Figure 2.4: The illustration of the propagation of focused beam.

research problem. Besides lateral resolution, temporal resolution is another significant property for ultrasound imaging. Therefore, the way to obtain a good lateral resolution image with good temporal resolution is of most interest.

In order to obtain a good lateral resolution, many beamforming methods are applied to ultrasound imaging. Some of them are listed below:

- **Dynamic Delay-and-Sum:** In this method, the focus is applied to each depth dynamically and the image is constructed with a montage process³, where image of focus zones are mounted together [2]. However, in such a method, multiple transmissions focusing on different depths are required, which reduces the temporal resolution of the imaging system. Assume the time for producing one scanline is τ s and the image is separated into κ focus zone and consists of M scanlines. In this case, the frame rate of producing an image is $1/(\tau\kappa M)$, which is κ times slower than producing an image with a single focus. This is a way of trading temporal resolution for spatial resolution that we mentioned in Introduction.
- **Parallel Beamforming:** Parallel Beamforming utilises a wide focused transmit beam and performs receive beamforming to form separate scanlines [4]. More scanlines can be formed from one transmission, which

³Montage process creates a composite image created by combining several separate images

can improve the temporal resolution without degrading the spatial resolution. Assuming that in each transmission, the wide transmission beam contains χ scanlines, the frame rate is $\chi/(\tau\kappa M)$. However, the curvature of the wide focused beam means that the scanline is also curved resulting in distortions in the reconstructed image.

- **Synthetic Aperture:** Synthetic aperture is a method widely studied by many researchers [47]. The main concept of synthesis aperture is to synthesize a large aperture by sequentially using small apertures. This method can dynamically focus the beam using the sequence information. As a result, focusing can be achieved with transmit focusing and temporal resolution is maintained with a frame rate $1/(\tau M)$. However, the low signal-to-noise ratio and low penetration from small apertures is a problem [48]. In this dissertation, the proposed method is implemented on the synthetic aperture method.
- **Ultrafast Imaging:** Recently, Montaldo *et al.* propose a coherent plane-wave compounding method [49], which is also called ultrafast ultrasound imaging. In this method, a plane wave with specific direction is transmitted and a low resolution image is reconstructed by receive focusing. By compounding the low resolution images with different transmission directions, a high resolution image is reconstructed. As the number of directions ϕ required are less than the number of scanline M , this method is $(\kappa M/\phi)$ times faster than the DAS method.

In all the methods above, focusing is a necessary process to obtain a high lateral resolution, or small mainlobe of ξ . However, the narrower the mainlobe, the higher the sidelobe will be. There are some data-independent apodisation methods like Hanning weights to reduce the sidelobe level. However, compared to data-independent apodisations, adaptive weights can achieve better resolution and off-axis interference suppression. Applying weights that vary with the sensor data to the aperture is referred to as adaptive beamforming. Some background knowledge on adaptive array beamforming will be given in the next section.

2.2 Adaptive Array Beamformer

2.2.1 Capon Beamformer

Capon minimum variance beamforming is an adaptive beamforming method based on the minimum variance criterion. Here, we will give a brief introduction on Capon beamformer; interested readers may refer to [20] for more details. Assuming we have M active elements receiving signals, the signal received by transducers are,

$$\mathbf{x}(t) = \mathbf{s}(t) + \sum_{j=1}^J s_j(t) + \mathbf{n}(t), \quad (2.14)$$

where $\mathbf{x}(t) = [x_1(t), x_2(t), \dots, x_M(t)]$ is the vector of signals received by M elements, j denotes the j th interference, J is the total number of interference and $\mathbf{s}(t)$ is,

$$\mathbf{s}(t) = s(t)\mathbf{a}(\theta, f), \quad (2.15)$$

where $\mathbf{a}(\theta, f) = [e^{i\theta}, e^{i2\pi\frac{d}{\lambda}\sin\theta}, \dots, e^{i2\pi(M-1)\frac{d}{\lambda}\sin\theta}]$ is the steering vector associated with the signal of interest as shown in Figure 2.5, where $\lambda = c/f$ is the wavelength of the signal. Note that, for broadband signals, the steering vector is frequency dependent and cannot be used directly. $\mathbf{s}_j(t) = s_j(t)\mathbf{a}(\theta_j, f)$ is the interference and $\mathbf{n}(t) = [n_1(t), n_2(t), \dots, n_M(t)]$ is the additive noise to the sensor array.

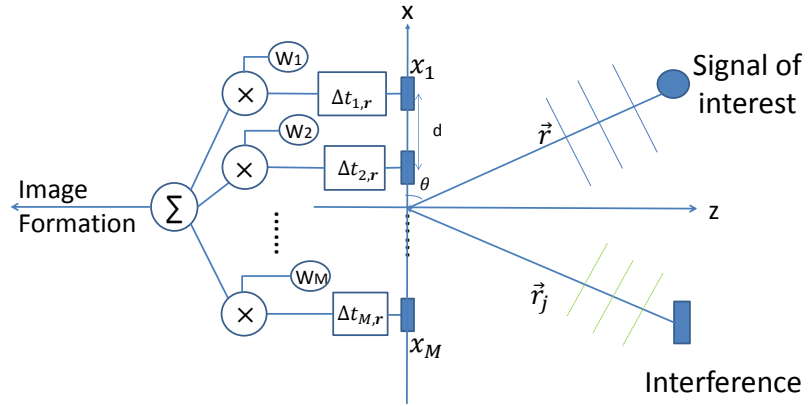


Figure 2.5: The illustration of an array system with farfield signal source and interference.

The output of the beamformer can be written as,

$$y(t) = \mathbf{w}^H \mathbf{x}(t), \quad (2.16)$$

where $\mathbf{w} = [w_1, w_2, \dots, w_M]$ is the apodisation weight vector. The aim of the adaptive beamformer is to compute the optimal apodisation weights \mathbf{w} . One way of obtaining the optimal weight \mathbf{w} is by maximizing the output Signal-to-interference-noise-ratio (SINR) of the beamformer. The output signal power is,

$$\begin{aligned} P_s &= E\{\mathbf{w}^H \mathbf{s}(t)\} (\mathbf{w}^H \mathbf{s}(t))^H \\ &= \mathbf{w}^H E\{\mathbf{s}(t) \mathbf{s}(t)^H\} \mathbf{w}, \end{aligned} \quad (2.17)$$

and the output interference and noise power is,

$$\begin{aligned} P_i &= E\{(\mathbf{w}^H \mathbf{s}_j(t) + n(t)) (\mathbf{w}^H \mathbf{s}_j(t) + n(t))^H\} \\ &= \mathbf{w}^H E\{(\mathbf{s}_j(t) + n(t)) (\mathbf{s}_j(t) + n(t))^H\} \mathbf{w} \end{aligned} \quad (2.18)$$

then, the output SINR of the beamformer is,

$$\text{SINR} = \frac{\mathbf{w}^H E\{\mathbf{s}(t) \mathbf{s}(t)^H\} \mathbf{w}}{\mathbf{w}^H E\{(\mathbf{s}_j(t) + n(t)) (\mathbf{s}_j(t) + n(t))^H\} \mathbf{w}} = \frac{|\mathbf{w}^H \mathbf{a}(\theta, f)| s(t)^2}{\mathbf{w}^H R_{j+n} \mathbf{w}}, \quad (2.19)$$

where $\mathbf{R}_{j+n} = E\{(\mathbf{s}_j(t) + n(t)) (\mathbf{s}_j(t) + n(t))^H\}$ is the interference-noise covariance matrix where j denotes the interference, n denotes the additive noise and $E\{\cdot\}$ denotes the expectation operator. The minimum variance distortionless response (MVDR) beamformer or Capon beamformer is obtained by minimizing the denominator, namely, the variance of interference and noise at output, while keeping the numerator fixed, namely, ensuring the distortionless response of the beamformer towards the direction of interest [50]. as a result, we have

$$\begin{aligned} &\underset{\mathbf{w}}{\text{minimize}} \mathbf{w}^H \mathbf{R}_{j+n} \mathbf{w}, \\ &\text{subject to } \mathbf{w}^H \mathbf{a}(\theta, f) = 1. \end{aligned} \quad (2.20)$$

Using the method of Lagrange multiplier, we get,

$$\mathcal{L}(\mathbf{w}, \lambda) = \mathbf{w}^H \mathbf{R}_{j+n} \mathbf{w} + \lambda (\mathbf{w}^H \mathbf{a}(\theta, f) - 1) \quad (2.21)$$

with Lagrange parameter, λ . The minimization problem in Equation 2.20 can be solved finding $\min_{\mathbf{w}} \mathcal{L}(\mathbf{w}, \lambda)$, where

$$\begin{aligned} \frac{\partial \mathcal{L}(\mathbf{w}, \lambda)}{\partial \mathbf{w}^H} &= \mathbf{w}^H R_{j+n} + \lambda \mathbf{a}(\theta, f) = 0 \\ \mathbf{w}^H &= -\lambda \mathbf{a}(\theta, f) \mathbf{R}_{j+n}^{-1}. \end{aligned} \quad (2.22)$$

Using the constraint on the weight vector in Equation 2.20, the Lagrange parameter λ is,

$$\lambda = -(\mathbf{a}(\theta, f)^H \mathbf{R}_{j+n}^{-1} \mathbf{a}(\theta, f))^{-1}. \quad (2.23)$$

Thus, the solution of this optimization problem is,

$$\mathbf{w}_{Capon} = \frac{\mathbf{R}_{j+n}^{-1} \mathbf{a}(\theta, f)}{\mathbf{a}(\theta, f)^H \mathbf{R}_{j+n}^{-1} \mathbf{a}(\theta, f)}, \quad (2.24)$$

From (2.24), we obtain the optimized adaptive weights to maximize the SINR. However, the interference-noise covariance matrix is not easy to obtain. In practice, the sample matrix inversion (SMI) is used instead of the interference-noise covariance matrix. SMI matrix is the inversion of the data covariance matrix $\mathbf{R}_{SMI} = E\{\mathbf{x}(t)\mathbf{x}(t)^H\}$. If the data set is large enough and the steering vector of the desired signal $\mathbf{a}(\theta)$ is precisely known, the SMI matrix \mathbf{R}_{SMI} can be used to substitute the interference-noise covariance matrix \mathbf{R}_{j+n} yielding,

$$\mathbf{R}_{SMI}^{-1} \mathbf{a}(\theta, f)^H = (\mathbf{R}_{j+n} + s(t)^2 \mathbf{a}(\theta, f)^H \mathbf{a}(\theta, f))^{-1} \mathbf{a}(\theta, f)^H \quad (2.25)$$

By using Sherman-Morrison formula, we have,

$$\begin{aligned} \mathbf{R}_{SMI}^{-1} \mathbf{a}(\theta, f)^H &= \left(\mathbf{R}_{j+n}^{-1} - \frac{\mathbf{R}_{j+n}^{-1} \mathbf{a}(\theta, f)^H \mathbf{a}(\theta, f) \mathbf{R}_{j+n}^{-1}}{1/s(t)^2 + \mathbf{a}(\theta, f)^H \mathbf{R}_{j+n}^{-1} \mathbf{a}(\theta, f)} \right) \mathbf{a}(\theta, f)^H \\ &= \left(\mathbf{R}_{j+n}^{-1} \mathbf{a}(\theta, f)^H - \mathbf{R}_{j+n}^{-1} \mathbf{a}(\theta, f)^H \frac{\mathbf{a}(\theta, f)^H \mathbf{R}_{j+n}^{-1} \mathbf{a}(\theta, f)}{1/s(t)^2 + \mathbf{a}(\theta, f)^H \mathbf{R}_{j+n}^{-1} \mathbf{a}(\theta, f)} \right) \\ &= \left(1 - \frac{\mathbf{a}(\theta, f)^H \mathbf{R}_{j+n}^{-1} \mathbf{a}(\theta, f)}{1/s(t)^2 + \mathbf{a}(\theta, f)^H \mathbf{R}_{j+n}^{-1} \mathbf{a}(\theta, f)} \right) \mathbf{R}_{j+n}^{-1} \mathbf{a}(\theta, f)^H, \end{aligned} \quad (2.26)$$

where $1 - \frac{\mathbf{a}(\theta, f)^H \mathbf{R}_{j+n}^{-1} \mathbf{a}(\theta, f)}{1/s(t)^2 + \mathbf{a}(\theta, f)^H \mathbf{R}_{j+n}^{-1} \mathbf{a}(\theta, f)}$ is only a coefficient which will be cancelled out in SINR. In the discussions later, we use \mathbf{R} instead of \mathbf{R}_{SMI} for simplicity. The result in Equation 2.25 holds true only when (i) the accuracy of data covariance matrix is high (large amount of data) and (ii) the steering vector is accurately known, we can use the sample matrix inversion instead of interference-noise covariance matrix which is not easy to obtain in practice. However, in practice, those two conditions are very hard to meet which deteriorates the beamformer. As a result, increasing the robustness of the Capon beamformer against limited data set and steering vector errors is significant.

In addition, if the interference is correlated with the signal of interest, in (2.26), the covariance matrix of interference cannot be separated from the signal covariance

matrix. Moreover, in a correlated signal case, the rank of signal subspace of the sample data matrix becomes one and as a result, the beamformer cannot suppress any interference at all [51]. Therefore, the way to improve the robustness against limited data set and steering vector errors and signal correlation is essential.

In Figure 2.6 and Figure 2.7, the Capon beamformer with uncorrelated signals and correlated signals are simulated. The number of transducers $M = 16$ with spacing $d = 0.2$ mm. The signal of interest is a plane wave with central frequency 3.5 MHz and 40% fractional bandwidth, coming perpendicular to the array and the interferences are plane waves from $\pi/6$ radians and $\pi/8$ radians.

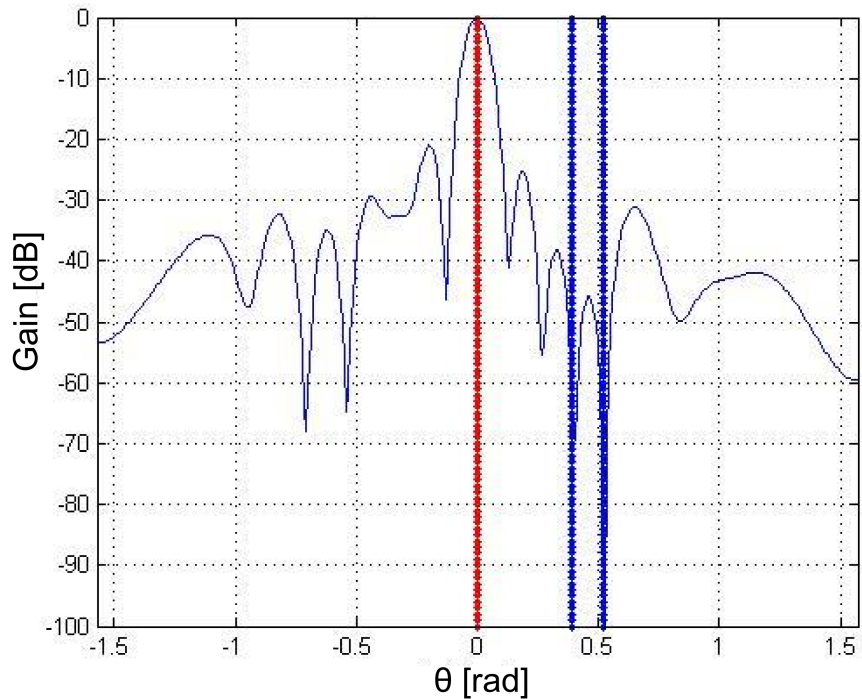


Figure 2.6: Beam Pattern of Capon beamformer with uncorrelated signals: signal from 0 radians and interference from $\pi/8$ and $\pi/6$ radians.

In Figure 2.6, we can see the performance of a Capon beamformer. Nullings, or suppressions, are found adaptively at the directions of interferences in the Capon beamformer. From Figure 2.7, we can observe that the signal correlation ruins the nulling formed by the Capon beamformer in the uncorrelated case and the interference cannot be suppressed properly. Hence, A decorrelation process is necessary for scenarios with correlated signals.

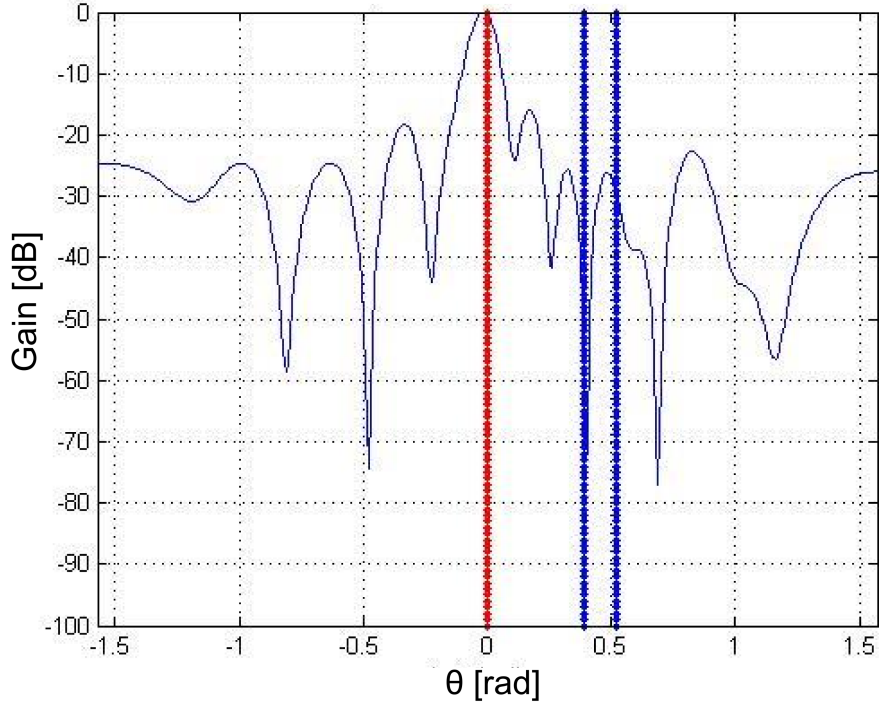


Figure 2.7: Beam Pattern of Capon beamformer with correlated signals: signal from 0 radians and interference from $\pi/8$ and $\pi/6$ radians.

2.2.2 Steering Vector Errors

In this section, we will outline some typical robust Capon beamformer (RCB) using linear constraint minimum variance (LCMV) method, diagonal loading (DL) method and eigenspace-based (ESB) method:

- **Linear Constraint Minimum Variance (LCMV):**

In (2.20), we derived the Capon minimum variance distortionless beamformer.

In order to increase its robustness against the steering vector errors, we change the distortionless condition to a linear constraint condition and formulate our optimizing problem as,

$$\begin{aligned} & \underset{\mathbf{w}}{\text{minimize}} \quad \mathbf{w}^H \mathbf{R} \mathbf{w}, \\ & \text{subject to } \mathbf{C}^H \mathbf{w} = \mathbf{g}, \end{aligned} \quad (2.27)$$

where $\mathbf{C} = \begin{bmatrix} \mathbf{a}(\theta_1) \\ \vdots \\ \mathbf{a}(\theta_\varsigma) \end{bmatrix}$ is the ς steering vectors to be constrained, and $\mathbf{g} = [g_1, \dots, g_\varsigma]$ is the constraint condition. Some typical are directional constraints that \mathbf{g} is a vector of 1 and the constrained steering vectors are the pos-

sible directions of the signal of interest, null constrains that $\mathbf{g} = [1, 0, \dots, 0]$ and the constrained steering vectors corresponding to 0 will be nulled out and derivative constraints which give the constraints on the derivatives of the steering vectors. In addition, a widely used method called generalised sidelobe canceller [52] is another type of linear constraint on the signal subspace. The main disadvantage of these LCMV methods are the required knowledge of specific steering vector condition.

- **Diagonal Loading (DL):**

The diagonal loading method comes from the quadratic constraints. Li et al proved the equivalence of adding the quadratic constraints on the weight vector and steering vector [53]. Here, we apply the a quadratic constraint on the weight vector and form the optimizing problem,

$$\begin{aligned} & \underset{\mathbf{w}}{\text{minimize}} \quad \mathbf{w}^H \mathbf{R} \mathbf{w}, \\ & \text{subject to } \mathbf{w}^H \mathbf{a}(\theta, f) = 1, \\ & \text{and } \|\mathbf{w}\|^2 \leq L, \end{aligned} \quad (2.28)$$

where $\|\cdot\|$ denotes the vector norm and L is a design parameter. The solution of this optimizing problem is,

$$\mathbf{w}_{DL} = \frac{(\mathbf{R} + \epsilon \mathbf{I})^{-1} \mathbf{a}(\theta, f)}{\mathbf{a}(\theta, f)^H (\mathbf{R} + \epsilon \mathbf{I})^{-1} \mathbf{a}(\theta, f)}, \quad (2.29)$$

where \mathbf{I} is identity matrix and ϵ is a parameter dependent on L . As the solution to this optimizing problem is only by adding a diagonal matrix to the covariance matrix in Capon beamformer, we usually call this method diagonal loading method. In this method, the main problem is determining the parameter ϵ (or L) is not a trivial problem. In this dissertation, we use the power of the received signal to determine ϵ [54], the detail method is illustrated in Chapter 3.

- **Eigenspace-based (ESB) Method:**

In the discussion of Capon beamformer in Section 2.2.1, we use sample matrix inversion instead of inversion of interference-noise matrix for practical use. However, the accuracy of \mathbf{R} is low. The space spanned by the eigenvectors of \mathbf{R} may be partitioned into the signal subspace \mathbf{R}_s and the noise subspace \mathbf{R}_n . The use of signal subspace is more accurate and the computational

complexity is low. Assuming the sample inversion matrix can be written as,

$$R_{SMI} = \mathbf{U}_{s+i}\Lambda_{s+i}\mathbf{U}_{s+i}^H + \mathbf{U}_n\Lambda_n\mathbf{U}_n^H, \quad (2.30)$$

where $\mathbf{U} = [\mathbf{U}_{s+i}, \mathbf{U}_n]$ is the eigenvector of \mathbf{R} and \mathbf{U}_n is orthogonal to \mathbf{U}_{s+i} and $\Lambda = \text{diag}[\Lambda_{s+i}, \Lambda_n]$ is the diagonal matrix of eigenvalues. Then,

$$R_{SMI}^{-1} = \mathbf{U}_{s+i}\Lambda_{s+i}^{-1}\mathbf{U}_{s+i}^H + \mathbf{U}_n\Lambda_n^{-1}\mathbf{U}_n^H. \quad (2.31)$$

As a result, the eigenspace-based Capon beamformer can be written as,

$$\mathbf{w}_{ESB} = \frac{\mathbf{U}_{s+i}\Lambda_{s+i}^{-1}\mathbf{U}_{s+i}^H\mathbf{v}(\vartheta)}{\mathbf{v}(\vartheta)^H\mathbf{U}_{s+i}\Lambda_{s+i}^{-1}\mathbf{U}_{s+i}^H\mathbf{v}(\vartheta)}. \quad (2.32)$$

The main drawback of this method is that the rank of signal subspace is required but hard to obtain correctly.

Besides these three typical methods to increase the robustness of adaptive beamformer, there are many other newly developed RCB methods like outage properties approach [55] and covariance fitting approach [56]. Most of these methods are based on convex optimisation theory and cannot be expressed in closed-form.

2.2.3 Correlated Signals

The interference discussed so far is not correlated with the signal of interest. However, in cases like multipath propagation, the interference is a scaled and delayed version of the interested signal. The data-dependent beamformers will lead to cancellation of the desired signal due to the highly correlated interference. To prevent the cancellation of correlated signals, there are various methods proposed for applications other than medical ultrasound imaging. The most widely used are (i) spatial smoothing and (ii) frequency smoothing methods. Spatial smoothing decorrelates the matrix by averaging the data covariance matrices over subarrays [51],

$$\overline{\mathbf{R}}_{\text{spatial}} = \frac{1}{M-L+1} \sum_{\ell=1}^{M-L+1} \mathbf{R}_\ell, \quad (2.33)$$

where \mathbf{R}_ℓ is the covariance matrix of the subarray $[x_\ell, \dots, x_{\ell+L}]$. Here, \mathbf{R}_ℓ can be calculated from both time domain data and frequency domain data. Then the

Capon beamformer with spatial smoothing (CB-SS) is,

$$\mathbf{w}_{CB-SS} = \frac{\mathbf{R}_{\text{spatial}}^{-1} \mathbf{a}(\theta, f)}{\mathbf{a}(\theta, f)^H \mathbf{R}_{\text{spatial}}^{-1} \mathbf{a}(\theta, f)}. \quad (2.34)$$

The output of this beamformer is,

$$y(t) = \frac{1}{L} \sum_{l=1}^L \mathbf{w}_{CB-SS}^* \mathbf{x}_l(t), \quad (2.35)$$

where $(\cdot)^*$ denotes the conjugate operator.

From the output, we can see that the aperture size is reduced due to using a subarray. In the meantime, the closely spaced interference cannot be decorrelated properly by spatial smoothing [24]. Compared to spatial smoothing, frequency smoothing does not reduce the aperture size. The detailed discussion on the frequency smoothing method and how to implement it for medical ultrasound imaging system is given in Chapter 3.

2.3 Adaptive Beamformer Applied to Ultrasound Imaging

In recent years, many researchers are working on applying adaptive Capon beamformer to medical ultrasound imaging. In 2002, Mann and Walker [7] applied a constrained adaptive beamformer to medical ultrasound imaging. This is the first time adaptive array beamforming is applied to ultrasound imaging for suppressing the off-axis interference. However, the use of single point target does not reveal the signal correlation problem.

In 2005, Sasso and Bacrie proposed the Capon beamformer combined with subarray averaging and consecutive transmission lines averaging [8]. This approach can effectively solve the signal correlation problem in medical ultrasound imaging and a better image quality is obtained. However, there are still some disadvantages of this method: (i) the spatial resolution will be reduced by using a subarray; (ii) the broad bandwidth used in ultrasound imaging is not utilised; (iii) the beamformer is not robust against small data set and steering vector error.

In the same year, Synnevåg *et al.* demonstrated a spatial smoothed robust Capon beamformer with a diagonal loading method [54], which increases the robustness of the beamformer. They examined their beamformer by experimental data of wire targets and a heart phantom. They observed a reduced mainlobe

width and better suppression of sidelobes compared to a DAS beamformer. Wang *et al.* applied a synthetic aperture method and averaged the spatial covariance matrix over single transmissions at different positions [22]. They evaluated their methods using experimental data including wire targets, cyst and heart phantoms. This method decorrelates the signal without sacrificing the aperture size. However, single transmissions suffer from low SNR. In 2007, Holfort *et al.* investigated a sub-band beamforming method in frequency domain [14] to utilise the broad bandwidth of ultrasound pulse; however, the performance of this method is limited by the low signal-to-noise ratio (SNR) of single sub-bands.

All of these literatures are initial works on implementation of Capon beamformer to improve the lateral resolution of the reconstructed medical ultrasound images. In order to increase the robustness of the beamformer, generalised side-lobe canceller (GSC) proposed by Khezerloo *et al.* [9] in 2009 and eigenspace based (ESB) beamformer proposed by Megduzadeg *et al.* [13] in 2012 and Asl *et al.* [57] in 2010 are applied to ultrasound imaging. Compared to diagonal loading, GSC method can achieve a better image quality but the complexity of the beamformer will be much higher. Megduzadeg *et al.* showed that ESB method can enhance edges and reduce noise but the speckle pattern can be distorted. Asl *et al.* found that ESB method can reduce sidelobes and improve contrast.

Compared to forward only spatial smoothing, forward-backward spatial smoothing is another decorrelation method which can achieve a better estimation of covariance matrix. Asl *et al.* [58] proposed a forward-backward Capon beamformer applied to ultrasound imaging and achieves a better resolution compared to forward-only method. However, the forward-backward spatial smoothing also utilises a subarray, which reduces the resolution.

Most of the adaptive beamformers above are applied to the typical scanline imaging system. However, temporal resolution is important for medical ultrasound system and high frame-rate imaging like parallel receive and coherent plane wave imaging is of great interest by researchers. Synnevåg *et al.* [59], Wang *et al.* [60] and Holfort *et al.* [61] applied the Capon beamformer to high frame rate ultrasound imaging. In high frame rate imaging system, the lateral resolution is sacrificed to increase the temporal resolution. However, by applying the Capon beamformer to high frame rate imaging, the temporal resolution is improved without sacrificing the lateral resolution as shown in these literatures.

Besides spatial resolution and temporal resolution, the computational complexity of the beamformer is important for medical ultrasound imaging. The computational complexity of a Capon based beamformer is $O(M^3)$, where M is the aperture

size, which is much higher than a DAS beamformer ($O(M)$). As a result, Synnevåg *et al.* [62] and Asl *et al.* [63] proposed a low-complexity adaptive beamformer for ultrasound imaging. The computational complexity of the beamformer is $O(M^2)$ but the beamformer significantly outperforms the DAS beamformer.

In recent years, 3D medical ultrasound imaging is a significant research topic. In 2013, Asl *et al.* [46] proposed an initial study on implementing the Capon beamformer onto the 3D medical ultrasound system.

2.4 Summary

This chapter provided an introduction to both ultrasound physics and adaptive array beamforming. Furthermore, we reviewed the application of adaptive array beamforming applied to medical ultrasound imaging. (i) In the ultrasound physics sections, the wave transmitted was described. After that, the interactions between the wave and the medium during wave propagation was introduced. The transmit and receive methods used to mitigate the effects of these interactions were introduced. Finally, the image formation methods were illustrated. (ii) In the adaptive array beamforming section, the Capon beamforming was first introduced and the approaches to increase the robustness against steering vector errors and correlated signals were discussed. (iii) In the last section, we reviewed the recent researches on adaptive array beamforming applied to medical ultrasound. In the next chapter, we will propose our adaptive array beamforming method applied to medical ultrasound imaging.

Chapter 3

Frequency Smoothed Robust Capon Beamformer

3.1 Introduction

In this chapter, we aim to demonstrate the performance of the proposed frequency smoothed robust Capon beamformer applied to medical ultrasound imaging. The technique is built on the background knowledge on adaptive array ultrasound imaging described in Chapter 2. Specifically, we wish to maximise the spatial resolution of the image and investigate the reconstruction quality of our frequency smoothed robust Capon beamformer with short observation time.

Firstly, we describe the problem of adaptive beamforming on broadband correlated signals. Following that, we propose a novel method, robust Capon beamformer with frequency smoothing (RCB-FS) to solve the problem. After that, we include some proofs on signal decorrelation by the proposed method. Simulations and discussions on the proposed method are also included, along with the evaluation metrics used to analyse the experimental results.

Then, we examine our proposed method using the experimental data from the Biomedical Ultrasonics Laboratory, University of Michigan at Ann Arbor [29]. The ultrasound RF data was collected using a complete set synthetic aperture focusing technique (SAFT), which means the signal is transmitted by a single transducer element and received by all the elements. We implemented fixed focus on transmission and dynamic focus on reception by delaying and summing the received signals from different transmitters. Next, the three beamforming algorithms (Golden DAS, RCB-SS and RCB-FS) mentioned in Chapter 2 were applied on the data and their performances compared. In the implementation of the RCB-FS method, a short observation time method, RCB-FS-short, to maximise the spatial resolution and a

long observation time method, RCB-FS-long, to provide more frequency sub-bands, can be used. As the spatial resolution is the property we focus on in this chapter, we only investigate the property of RCB-FS-short in this chapter. The design parameters are chosen by experimental optimisation when the proposed algorithms are implemented onto the ultrasound data:

- In spatial smoothing, we chose a sub-aperture width equal to half of the full aperture.
- For frequency smoothing, we chose the length of the time segment equal to the length of the excitation pulse.
- The diagonal loading factor was chosen with $\sigma = 1/10$ to get a well conditioned covariance matrix.

After beamforming, envelope detection, gain compensation, logarithmic compression and scan conversion were sequentially applied. Furthermore, all the reconstructed images in this dissertation were displayed over a 45 dB dynamic range.

3.2 Problem Formulation

We assume an M elements active array, each transmitting a broadband pulse of bandwidth B Hz to focus at the point of interest \mathbf{r} as shown on Figure 2.5. These pulses are reflected back by scatterers and recorded by the same M elements simultaneously. To image the whole area, transmission and reception are repeated by moving the focal point throughout the whole region of interest. The recorded signals at time t from the m th elements when the transmissions are focused at position \mathbf{r} is the sum of three terms

$$x_m(t, \mathbf{r}) = s_{0,m}(t, \mathbf{r}) + \sum_{j=1}^J s_{j,m}(t, \mathbf{r}_j) + n_m(t, \mathbf{r}) \quad (3.1)$$

where $s_{0,m}(t, \mathbf{r})$ is the signal of interest from position \mathbf{r} received by element m , $s_{j,m}(t, \mathbf{r})$ are the J interference signals due to reflections from the off-axis directions \mathbf{r}_j and $n_m(t, \mathbf{r})$ is the noise which is independent from the signals, and mainly includes random Gaussian noise and speckle noise. The latter two terms in (3.1) are residual terms to be minimized.

The M receiving channels are pre-steered to sum in phase the signal originating

from the focal point \mathbf{r} . The output of a general beamformer is,

$$y(t, \mathbf{r}) = \mathbf{w}(\mathbf{r})^H \tilde{\mathbf{x}}(t, \mathbf{r}) \quad (3.2)$$

where $(\cdot)^H$ denotes the transpose conjugate operator. Here,

$$\tilde{\mathbf{x}}(t, \mathbf{r}) = [x_0(t - \Delta t_{0,\mathbf{r}}), \dots, x_{M-1}(t - \Delta t_{M-1,\mathbf{r}})]^T \quad (3.3)$$

is the delayed version of received time domain signal matrix

$$\mathbf{x}(t) = [x_0(t, \mathbf{r}), \dots, x_{M-1}(t, \mathbf{r})]^T, \quad (3.4)$$

$\Delta t_{m,\mathbf{r}}$ are the time delays to focus at the point of interest \mathbf{r} and $(\cdot)^T$ denotes the transpose operator. The weights,

$$\mathbf{w}(\mathbf{r}) = [w_0(\mathbf{r}), \dots, w_{M-1}(\mathbf{r})] \quad (3.5)$$

where $w_m(\mathbf{r})$ is the weight applied to the m th element.

To estimate the signal $s_0(t)$, the weights $w_m(t)$ has to be optimized to maximize the desired signal. The Capon adaptive beamformer is usually applied to optimize the array output when the direction of arrival is precisely known. The Capon beamformer is formulated as

$$\begin{aligned} & \underset{\mathbf{w}(\mathbf{r})}{\text{minimize}} \quad \mathbf{w}(\mathbf{r})^H \mathbf{R}(\mathbf{r}) \mathbf{w}(\mathbf{r}), \\ & \text{subject to } \mathbf{w}(\mathbf{r})^H \mathbf{a}(\mathbf{r}) = 1, \end{aligned} \quad (3.6)$$

where $\mathbf{R}(\mathbf{r}) = E\{\mathbf{x}(\mathbf{r})\mathbf{x}(\mathbf{r})^H\}$ is the spatial covariance matrix of the received data, $E\{\}$ denotes the expectation operator and $\mathbf{a}(\mathbf{r})$ is the steering vector to focus at the point of interest \mathbf{r} . From the expression above, the Capon beamformer minimize contribution from the interferences while maintaining unit gain from the desired direction. By the Lagrange multiplier method, the solution to the Capon beamformer is given by

$$\mathbf{w}(\mathbf{r}) = \frac{\mathbf{R}(\mathbf{r})^{-1} \mathbf{a}(\mathbf{r})}{\mathbf{a}(\mathbf{r})^H \mathbf{R}(\mathbf{r})^{-1} \mathbf{a}(\mathbf{r})}. \quad (3.7)$$

From the expression, the solution is ill-conditioned if the signal covariance matrix is singular. Signals are coherent due to multipath propagation. To obtain a full rank covariance matrix, the uncorrelated number of observations has to be no less than the number of spatial transducers M . These uncorrelated observations can come from different single transmissions [22] with low SNR, sub-arrays [10] with a

smaller aperture size and neighbour points [11] or a sector of points from a same depth [12] which is constrained by the condition that the amount of data must be less than the width of the pulse length. Since all these decorrelation methods more or less deteriorate the image quality, a new decorrelation method which is able to maintain a good image quality is needed.

3.3 Proposed Beamforming Method

3.3.1 Frequency Smoothing

Frequency smoothed covariance matrix

Frequency smoothed covariance matrix is obtained by averaging the spatial covariance matrix over different frequency bins

$$\bar{\mathbf{R}}(\mathbf{r}) = \frac{1}{K} \sum_{\ell=1}^K \mathbf{R}(k_\ell, \mathbf{r}) \Delta\omega, \quad (3.8)$$

where $\mathbf{R}(k_\ell, \mathbf{r}) = E\{\mathbf{X}(k_\ell, \mathbf{r})\mathbf{X}(k_\ell, \mathbf{r})^H\}$ is the pre-steered covariance matrix at wave number k_ℓ where $k_\ell = \frac{\omega_\ell}{c}$ and ω_ℓ is the central angular frequency of the ℓ th sub band, $\mathbf{X}(k_\ell, \mathbf{r}) = [X_0(k_\ell, \mathbf{r}), \dots, X_{M-1}(k_\ell, \mathbf{r})]^H$, where $X_m(k_\ell, \mathbf{r})$ is the fourier transform of $x_m(t, r)$, $\Delta\omega = \omega_{k_{\ell+1}} - \omega_\ell$, and K is the number of sub-bands. The more frequency bins we use, a more stabilized frequency smoothed covariance matrix we can obtain. However, when the level of smoothing is increased, more side lobes will be introduced. The pre-steered covariance matrix is used here to avoid the estimation errors of the focusing matrix. After the frequency smoothed covariance matrix is obtained, the optimal weights can be found by, ϵ_n

$$\mathbf{w}(\mathbf{r}) = \frac{\bar{\mathbf{R}}(\mathbf{r})^{-1}\mathbf{a}(\mathbf{r})}{\mathbf{a}(\mathbf{r})^H \bar{\mathbf{R}}(\mathbf{r})^{-1}\mathbf{a}(\mathbf{r})}. \quad (3.9)$$

RCB-FS-short

To obtain the frequency domain sub-band signals $\mathbf{X}(k_\ell, \mathbf{r})$, two implementation methods are considered. The first method is to use time domain pre-steering and short time Fourier transform (STFT). We call this method RCB-FS-short. In this method, we apply pre-steering to focus the time domain signals from different transducers to the point of interest and apply the short time Fourier transform over a small time interval $[0, N - 1]$,

$$\mathbf{X}(k_\ell, \mathbf{r}) = \sum_{t=0}^{N-1} \tilde{\mathbf{x}}(t, \mathbf{r}) e^{-i2\pi k_\ell t/N}. \quad (3.10)$$

In this method, the performance of the beamformer will be affected by the choice of observation time N . To obtain a full rank covariance matrix, the number of frequency bins N must be larger than the number of sensors M . Moreover, short observation times can minimize the interference signals outside the observation interval but it will deteriorate the beamformer due to the low signal-to-noise ratio. However, since a pre-steering is applied to focus the time domain signals at the point of interest, the signals far away from the focus point will be de-focused and minimized by the beamformer in most practical situations. Therefore, we proposed a second method.

RCB-FS-long

The whole time domain signals are transformed into frequency domain using discrete Fourier transform (DFT) and a proper phase factor is applied to focus at point \mathbf{r} ,

$$\mathbf{X}(k_\ell, \mathbf{r}) = \Psi(k_\ell, \mathbf{r}) \cdot \sum_{t=0}^{T-1} \mathbf{x}(t, \mathbf{r}) e^{-i2\pi k_\ell t/T} \quad (3.11)$$

where T is the length of the time domain signals from one scanline and $\Psi(k_\ell, \mathbf{r}) = [e^{-i2\pi \Delta t_{0,\mathbf{r}} k_\ell}, \dots, e^{-i2\pi \Delta t_{M-1,\mathbf{r}} k_\ell}]$ is the frequency dependent broadband phase factor to focus the array to position \mathbf{r} . In this method, a longer observation time is used and we call it RCB-FS-long. As more sub-bands are available in RCB-FS-long, further frequency domain implementations like frequency compounding becomes easier. Moreover, as the observation time is longer, the robustness of the beamformer is better compared to RCB-FS-short.

Beamformer Output

In ultrasound imaging, we are using the received signal to estimate the distribution of reflectivity as mentioned in Chapter 2. As a result, in order to obtain the reflectivity, we applied the structure shown in Figure 3.1 to form the output. The weights found by RCB-FS are applied to each subband. Then, the subband responses are summed to obtain the beamformer output as shown,

$$y(\mathbf{r}) = \frac{1}{KM} \sum_{\ell=1}^K \sum_{m=0}^{M-1} w_m(\mathbf{r}) X_m(k_\ell, \mathbf{r}). \quad (3.12)$$

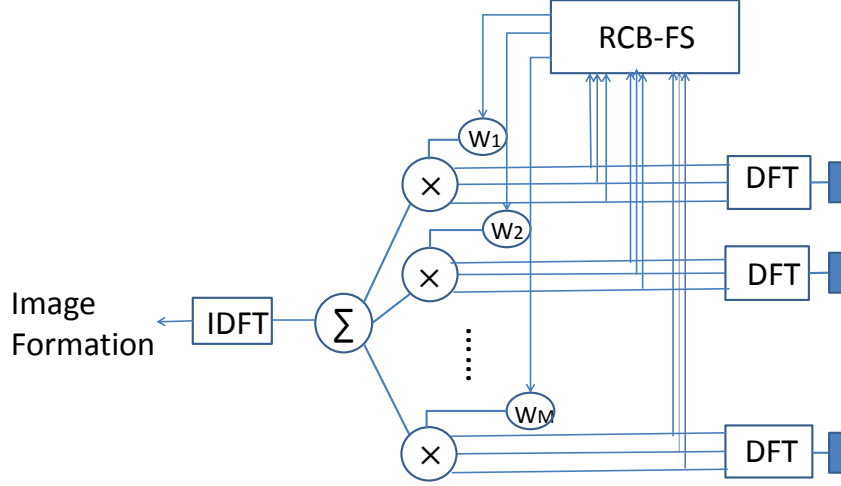


Figure 3.1: The block diagram of RCB-FS.

To estimate the reflectivity, envelope detection, logarithmic compression and scan conversion were applied to form a B-mode image.

Decorrelation of covariance matrix

The frequency smoothed spatial covariance matrix of received signal $x(t, \mathbf{r})$ can be re-written as,

$$\bar{\mathbf{R}}(\mathbf{r}) = \frac{1}{K} \left[\sum_{\ell=1}^K (\mathbf{R}_0(k_\ell, \mathbf{r})) + \bar{\mathbf{R}}_N(\mathbf{r}) \right] \quad (3.13)$$

where $\mathbf{R}_0(k_\ell, \mathbf{r})$ is the pre-steered sub-band spatial covariance matrix of signal $s(t)$ including signals $s_0(t, \mathbf{r})$ and $s_j(t, \mathbf{r})$. Note that $\mathbf{R}_0(k_\ell, \mathbf{r})$ may be singular at every frequency bins in a multipath propagation situation. $\bar{\mathbf{R}}_N(\mathbf{r}) = \sum_{\ell=1}^K \mathbf{R}_N(k_\ell, \mathbf{r})$ is the frequency-smoothed covariance matrix of the noise wavefield assumed to be independent from the signals,

$$\mathbf{R}_N(k_\ell, \mathbf{r}) = \mathbf{R}_j(k_\ell, \mathbf{r}) + \sigma_{k_\ell}^2 \mathbf{I}^2, \quad (3.14)$$

where $\mathbf{R}_j(k_\ell, \mathbf{r})$ comes from the frequency dependent speckle noise, σ is the gaussian noise level and \mathbf{I} is the identity matrix. Note that by frequency smoothing, the first term is reduced due to the summation of different speckle patterns in different sub-bands. In addition, the second term is more statistically stable. As a result, frequency smoothing can improve the robustness of the beamformer.

In multipath propagation, the interference is a delayed and scaled version of the

transmitted signal or signal of interest, hence, interference $s_j(t, \mathbf{r}) = \alpha_j s_0(t - \Delta t_j, \mathbf{r})$, where $j = 1, 2, \dots, J$, and Δt_j and α_j are the delay and the attenuation factor of the j th interference. In the multipath case, the rank of $\mathbf{R}_0(k_\ell, \mathbf{r})$ will become one and hence, the number of signal subspace will become one, which will ruin the beamformer. We will prove that if the interference is delayed sufficiently, then the frequency smoothed signal covariance matrix is full rank yielding,

$$\begin{aligned}
& \sum_{k_\ell=1}^K (\mathbf{R}_0(k_\ell, \mathbf{r})) \\
&= \sum_{k_\ell=1}^K E\{s(t)s(t)^H\} \\
&= \sum_{k_\ell=1}^K E\{S(k_\ell)S(k_\ell)^H\} \\
&= \sum_{k_\ell=1}^K \begin{bmatrix} S_0(k_\ell, \mathbf{r})^2 & S_0(k_\ell, \mathbf{r})S_1(k_\ell, \mathbf{r})^* & \cdots & S_0(k_\ell, \mathbf{r})S_J(k_\ell, \mathbf{r})^* \\ S_1(k_\ell, \mathbf{r})S_0(k_\ell, \mathbf{r})^* & S_1(k_\ell, \mathbf{r})^2 & \cdots & S_1(k_\ell, \mathbf{r})S_J(k_\ell, \mathbf{r})^* \\ \cdots & \cdots & \cdots & \cdots \\ S_J(k_\ell, \mathbf{r})S_0(k_\ell, \mathbf{r})^* & S_J(k_\ell, \mathbf{r})S_1(k_\ell, \mathbf{r})^* & \cdots & S_J(k_\ell, \mathbf{r})^2 \end{bmatrix} \quad (3.15)
\end{aligned}$$

where $S(k_\ell)$ is the fourier transform of $s(t)$. The correlations becomes,

$$C_0 = \sum_{k_\ell=1}^K S_0(k_\ell, \mathbf{r}_0)S_j(k_\ell, \mathbf{r}_j)^* \approx \int_B S_0(\omega, \mathbf{r}_0)S_0(\omega, \mathbf{r}_0)^*e^{-i\omega\tau_j}d\omega \quad (3.16)$$

Assuming a flat-spectrum in bandwidth B Hz,

$$S_0(\omega, \mathbf{r}) = \text{rect}\left(\frac{\omega}{B}\right), \quad (3.17)$$

by Wiener-Khinchin theorem [64],

$$\int_B S_0(\omega, \mathbf{r})S_0(\omega, \mathbf{r})^*e^{-i\omega\tau_j}d\omega = \text{sinc}(B\tau_j) \quad (3.18)$$

where $\text{sinc}(t) = \frac{\sin(t)}{t}$. When $\tau > 1/B$, the cross terms in the covariance matrix are negligible. Hence, if the interfering reflectors arrive $1/B$ seconds apart, then the correlation of the signals in the frequency smoothed covariance matrix is negligible.

Advantage of frequency smoothing

Frequency smoothing adaptive beamformer focuses the dispersion of frequencies improving the steering performance and at the same time eliminating coherence from multipath. Furthermore, for ultrasound imaging, the bandwidth B is very large meaning that even closely located reflectors are not coherent with frequency smoothing.

When it comes to spatial smoothing, the closely spaced reflectors cannot be decorrelated [24]. The noise from the overlap of sub-aperture in spatial smoothing is partially correlated; the average over different sub-arrays will induce some strong noise resulting in a correlated noise covariance matrix which deteriorates the performance of the beamformer. However, for frequency smoothing, the speckle patterns in different frequency bins are independent and the smoothing process will minimize the noise.

The performance of Capon beamformer with spatial smoothing and frequency smoothing is simulated in Figure 3.2 and Figure 3.3. The number of transducers $M = 16$ with spacing of 0.2 mm. The signal of interest is a plane wave with central frequency 3.5 MHz with 40% fractional bandwidth, coming perpendicular to the array and the interferences are plane waves from $\pi/6$ radians and $\pi/8$ radians. The interferences are correlated with the signal of interest. The length of the received signals is $1000\mu s$. In Figure 3.2, Capon beamformer with spatial smoothing is applied with a sub-array size $L = 4$. In Figure 3.3, Capon beamformer with frequency smoothing is applied.

From the figures, the mainlobe width of the Capon beamformer with spatial smoothing is much wider than the Capon beamformer with frequency smoothing as expected. More nullings can be formed by the frequency smoothing method as a larger number of transducers are available.

3.3.2 Diagonal Loading

The Capon beamformer will be mismatched and hence leading to a poor performance if:

- the size of the training set is small;
- the steering vector is not accurately known.

In order to improve the robustness of the beamformer against the above-mentioned cases, diagonal loading is applied to the proposed weighting vector as,

$$\mathbf{w}(\mathbf{r}) = \frac{(\bar{\mathbf{R}}(\mathbf{r}) + \epsilon \mathbf{I})^{-1} \mathbf{a}(\mathbf{r})}{\mathbf{a}(\mathbf{r})^H (\bar{\mathbf{R}}(\mathbf{r}) + \epsilon \mathbf{I})^{-1} \mathbf{a}(\mathbf{r})}, \quad (3.19)$$

where ϵ is a parameter that has to be optimized. Comparing (3.19) with the weights of the Capon beamformer given in (3.7), we can see that the diagonal loading method adds a regularization term to the covariance matrix, *i.e.*, replacing $\bar{\mathbf{R}}(\mathbf{r})$ with $\bar{\mathbf{R}}(\mathbf{r}) + \epsilon \mathbf{I}$. However, there exists no available method to optimally determine ϵ , which is the main problem in the application of diagonal loading. The parameter ϵ is commonly estimated from the power of the received signal, by evaluating $\epsilon = \eta \cdot \text{tr}\{\bar{\mathbf{R}}(\mathbf{r})\}$ where $\text{tr}\{\cdot\}$ is the trace operator and η is a constant which is a design parameter.

In Figure 3.4, the proposed robust Capon beamformer with diagonal loading is simulated. The number of transducer is $M = 16$ with spacing 0.2 mm. The signal of interest is a plane wave with central frequency 3.5 MHz with 40% fractional bandwidth, coming perpendicular to the array and the interferences are plane waves from $\pi/6$ radians and $\pi/8$ radians. The interferences are correlated with the signal of interest. The length of the received signals is $1000\mu\text{s}$. The proposed RCB-FS beamformer is applied to the received signals. The parameter η is optimized to be 0.1.

From the figure, we can see that the interferences are suppressed properly by the proposed beamformer without being ruined by the signal correlations as shown in Figure 3.3. Due to the robustness of the diagonal loading, the beamformer is similar to a DAS beamformer in Figure 1.4. But the suppression of interference is done adaptively similar to the Capon beamformer in Figure 2.6. The performance of beamformers shown in Figure 3.3 and Figure 3.4 does not differ a lot. This is due to the large training data set available in the simulation, but this is not the case in medical ultrasound imaging. As a result, diagonal loading is essential to increase the robustness of the beamformer.

3.3.3 Computational Complexity

In ultrasound imaging, the computational complexity is significant. In our RCB-FS-short method, for each focus point, we need to perform DFT for all sensors with computational order $O(M^2 \log M)$ and the RCB that has computational complexity of $O(M^3)$; therefore, the computational order of RCB-FS-short is $O(M^2 \log M) + O(M^3) = O(M^3)$ and it is the same as that of RCB-SS method ($O(M^3)$). For RCB-

FS-long method, it has same computational complexity but easier to implement since initial segments of received data are not needed but the whole data is used.

3.4 Evaluation Metrics

Spatial resolution is a metric to determine how closely an ultrasound system can discriminate scatterers. The axial resolution of the ultrasound system is determined by the structure of the transducer and the lateral resolution is determined by the beamforming algorithm, which is what we are going to evaluate. Lateral resolution is a metric, which is hard to quantify in ultrasound imaging. Normally, we use the full width at half maximum (FWHM) and the peak-side-lobe level (PSL) as shown in Figure 3.5 to quantify the lateral resolvable ability of the algorithm. In theory, for a linear array with length L and signal wavelength λ , the Rayleigh resolution limit can be found by $\sin^{-1}(\frac{\lambda}{L})$ [65].

3.5 Wire Targets

We applied the three methods on experimental data for six wire targets to compare the resolution of the different methods. The wires were placed at axial distances of 34, 48, 65, 83, 101 and 121 mm. The ultrasound data was collected by 128 transducers with central frequency 3.5 MHz, and sampled at 13.8889 MHz.

3.5.1 Overal Image Quality

From Figure 3.6, for the first set of reconstructions, we used the full aperture (128 transducers) to transmit and receive. (a), (b) and (c) are reconstructed using DAS, RCB-SS and RCB-FS-short respectively. For the second set of reconstructions, we used only half of the aperture to form the image. The lower less aperture size can reduce the computational complexity, temporal resolution and increase the manipulability - more flexible to detect small area. We examine the performance of the algorithms using half aperture in (d), (e) and (f).

We can observe that all of the three algorithms have a good performance when using a full aperture. However, the size of the wire targets, in RCB-FS-short is smaller than those in RCB-SS and DAS, which means both the lateral and axial resolution is better in the proposed method. The wire target reconstruction is sharper in RCB-FS-short as the intensities are more concentrated. All of the three algorithms performs well for sidelobe suppression when using a full aperture.

However, if we use the central 64 transducers (half aperture) to transmit and receive signals as shown in Figure 3.6 (d), (e) and (f), the RCB-FS-short again performs better than the other two algorithms. We observe some shadow from sidelobes in DAS and RCB-SS while we can obtain clear wire targets in RCB-FS-short.

The most interesting finding is that the performance of RCB-FS-short with half aperture is as good as the other two beamforming methods using full aperture, with a similar sidelobe level, but a slightly larger mainlobe width.

For quantitatively analysis, we look at the Table 3.1. From the table, we can

Method	Element	FWHM (deg.)	PSL (dB)
DAS	128	0.98	- 46
RCB-SS	128	0.91	- 46
RCB-FS	128	0.56	- 50
DAS	64	1.75	- 40
RCB-SS	64	1.68	- 41
RCB-FS	64	1.05	- 46

* The Rayleigh resolution limit for 128 elements is 0.86 degree.

* The Rayleigh resolution limit for 64 elements is 1.72 degree.

Table 3.1: Average FWHM and PSL of different algorithms using full aperture

see that for the 128 transducers case, the average Full Width at Half maximum (FWHM) of RCB-FS-short is 0.4 degree narrower than that in the other two algorithms and the Peak Side-lobe Level (PSL) of RCB-FS-short is 4dB lower than that in the other two algorithms.

3.5.2 Analysis

To look at the performance of the beamformer in detail, we plot the lateral variation, or beam pattern of wire targets at depth 48 mm and 83 mm using a half aperture size (see Figure 3.7).

From the beam pattern, we can see that the mainlobe width is small for the proposed method. From Figure 3.7 (a), we can see the proposed method is very close to the DAS method but the peak of RCB-SS method is slightly steered. As a result, the sidelobe of the RCB-SS beamformer is high in this case. For (b), three methods have good signal enhancement in the look direction, but the proposed method has the narrowest mainlobe as expected. The fluctuation of the beam pattern comes from the background noise of the experimental data.

In frequency domain processing, a small observation time and overlapping of

the signals will ruin the axial resolution; therefore, we compared the axial variation of the three methods with half aperture at 52° (74th scanline) (see Fig 3.8). The reason for choosing the 74th scanline is because of the presence of the fifth wire target.

Here, we observe that the axial resolution is not deteriorated in RCB-FS-short. Moreover, we can see that the interference from other peaks (34, 65, 83 and 121 mm) are suppressed better in RCB-SS and RCB-FS-short as expected - between RCB-SS and RCB-FS-short, at points 48 mm and 65 mm in Figure 3.8, RCB-SS performs better while other points do not; but their performance is almost the same. The fluctuation in the proposed method is smaller compared to the other two methods.

3.6 *Gearbr* Phantom

We applied our algorithm on experimental data of a *Gearbr* phantom [29] to see the resolution between different algorithms for imaging a complicated biomedical structure. Here, we only compared the image quality between RCB-SS and RCB-FS-short. The image data was collected by 64 transducers with central frequency 3.333 MHz, at 17.76 MHz sampling frequency. The reconstructed images are shown in Fig. 3.9.

From the reconstructed wire targets in the *gearbr* phantom, we can see the axial and lateral resolution in RCB-FS-short is better than that in RCB-SS. The FWHM of the proposed method is 0.5 degree narrower than RCB-SS. As the depth of the wire target is deep, the size difference of the wire targets in the reconstructed image is huge. The sidelobe level of the proposed method is 5 dB less than RCB-SS.

In addition, the speckle at lower depths in RCB-FS-short is less than in RCB-SS and the contrast of the lesion to the background is higher in the proposed method. The boundary of the lesions are better defined for the proposed method. More detailed quantitative analysis on speckle and contrast will be conducted in the next chapter. Moreover, the image reconstruction at higher depths is much better in RCB-FS-short compared to RCB-SS.

3.7 Discussions

From the results of the wire targets and *gearbr* phantom, the image quality, especially lateral resolution of the proposed RCB-FS-short is better than that of RCB-SS due to a larger effective aperture size. Moreover, the possibility of re-

ducing the aperture while keeping a good image quality in wire target experiments enables a reduction on the data storage memory and increases the frame rate (temporal resolution), which has a great benefit. Further implementation on synthetic aperture and ultrafast imaging can be considered. Furthermore, the proposed high resolution RCB-FS-short method has a computational complexity similar to the Capon beamformer based methods.

From the *gearb* phantom results, we can see the speckle is reduced. As we know, the speckle comes from the interference due to sub-resolution scatterers, and this interference differs in different frequencies. The frequency smoothing process can reduce the speckle in a similar fashion as frequency compounding since it uses information from different frequencies. Moreover, in Fig. 3.9, the good resolution in the far end in RCB-FS-short means a high penetration depth for RCB-FS-short which also comes from a large aperture size and utilization of different frequency information.

3.8 Summary

In this chapter, we proposed an RCB-FS-short beamforming method for maximising spatial resolution for ultrasound imaging. This RCB-FS adaptive beamforming algorithm suppresses the offset interference with a full utilization of the aperture size and the large bandwidth. We examined our RCB-FS-short method using experimental data. It showed narrower mainlobe width and lower sidelobes when compared to RCB-SS and DAS methods. Additionally, the speckle is reduced for our method which also provides better image reconstruction at higher depths. In order to further improve the image quality and utilize the proposed method in other areas, we combine our method with frequency compounding and try to obtain a better speckle reduction reconstruction in the next chapter.

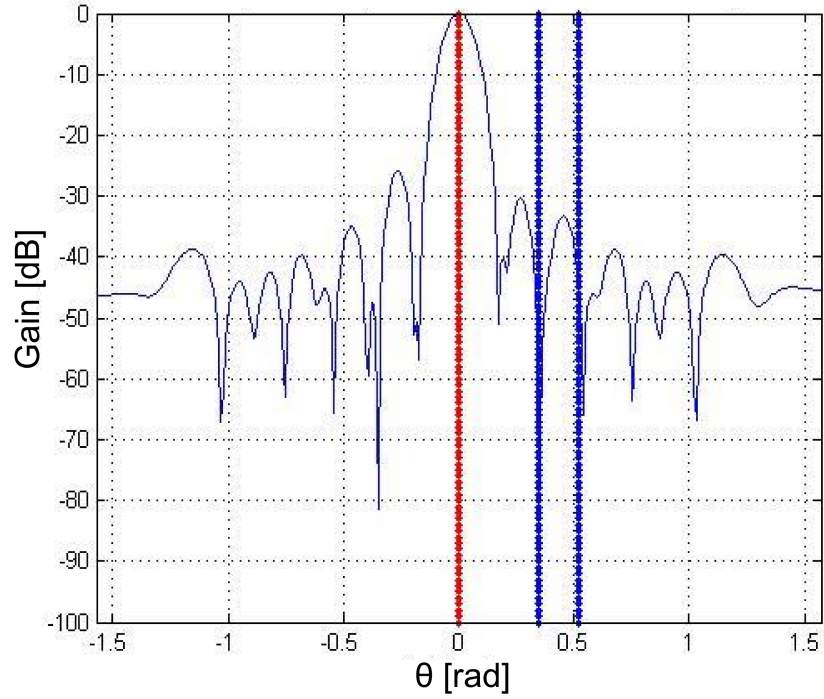


Figure 3.2: The beam pattern of Capon beamformer with spatial smoothing: signal from 0 radians and interference from $\pi/8$ and $\pi/6$ radians.

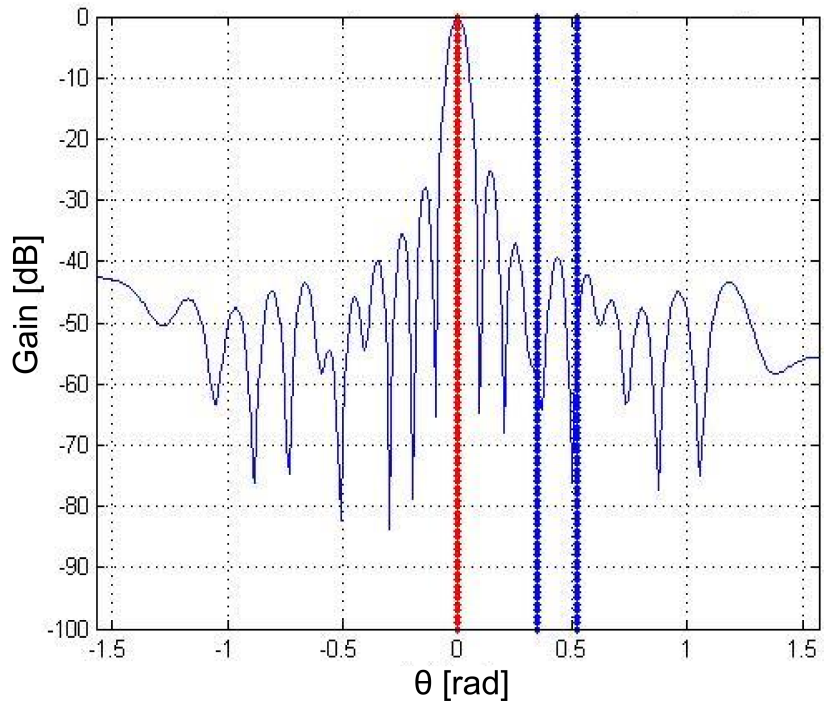


Figure 3.3: The beam pattern of Capon beamformer with frequency smoothing: signal from 0 radians and interference from $\pi/8$ and $\pi/6$ radians.

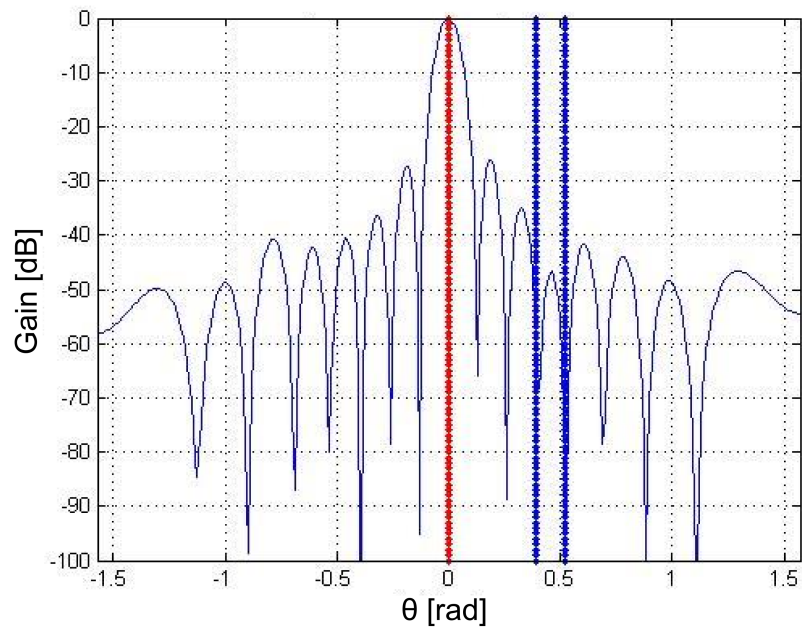


Figure 3.4: The beam pattern of robust Capon beamformer with frequency smoothing and diagonal loading: signal from 0 radians and interference from $\pi/8$ and $\pi/6$ radians.

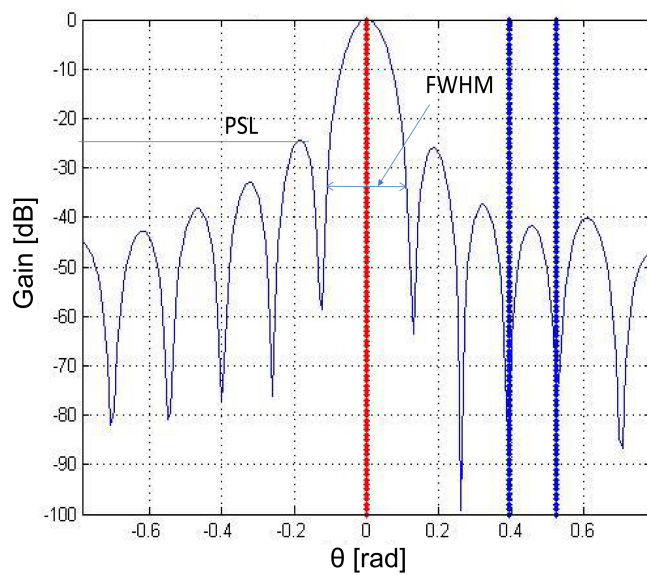


Figure 3.5: Illustration of FWHM and PSL.

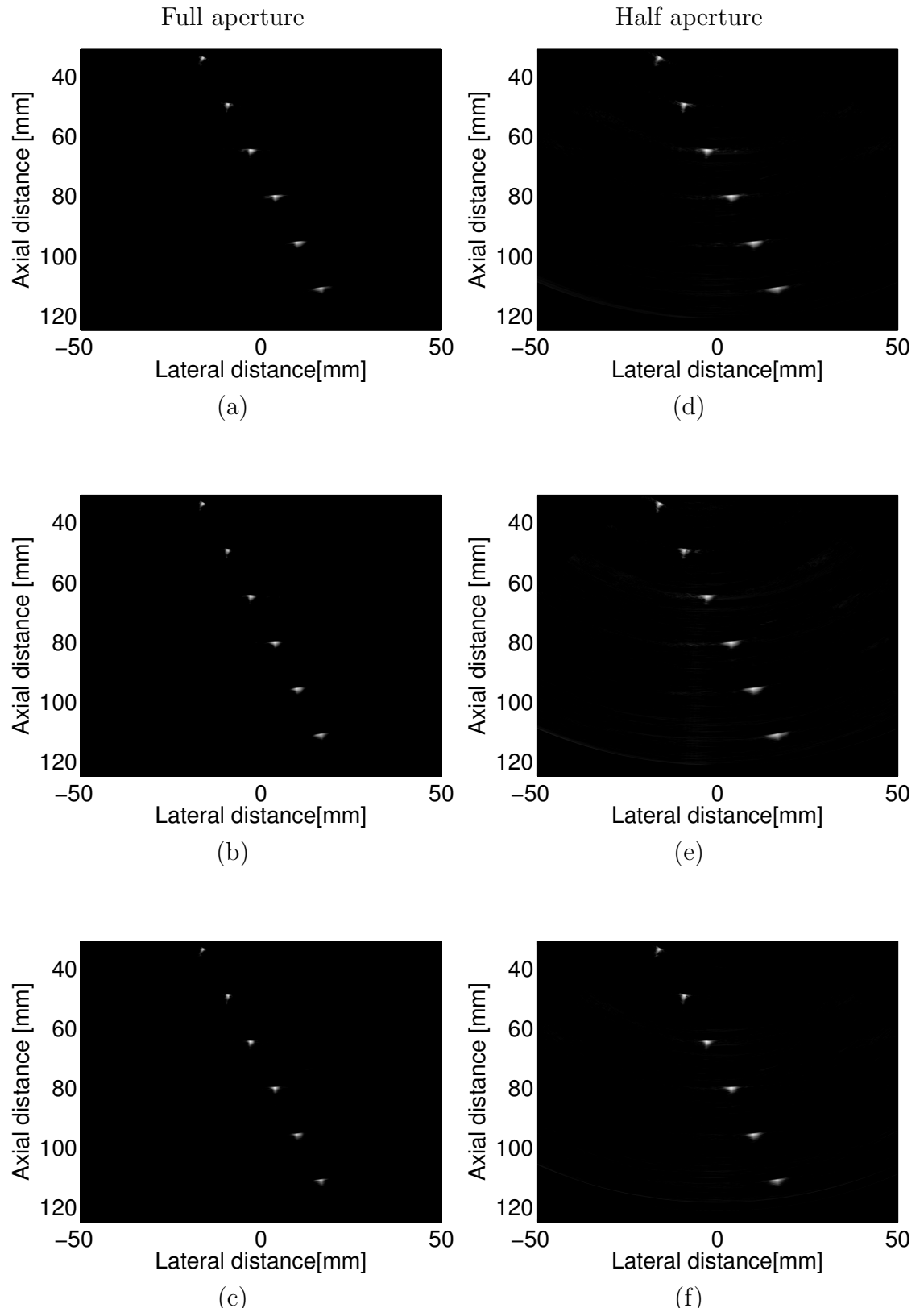


Figure 3.6: Images obtained from experimental data of wire targets: (a) DAS, (b) RCB-SS and (c) RCB-FS-short using the full aperture. Images obtained from (d) DAS, (e) RCB-SS and (f) RCB-FS-short using only half the aperture.

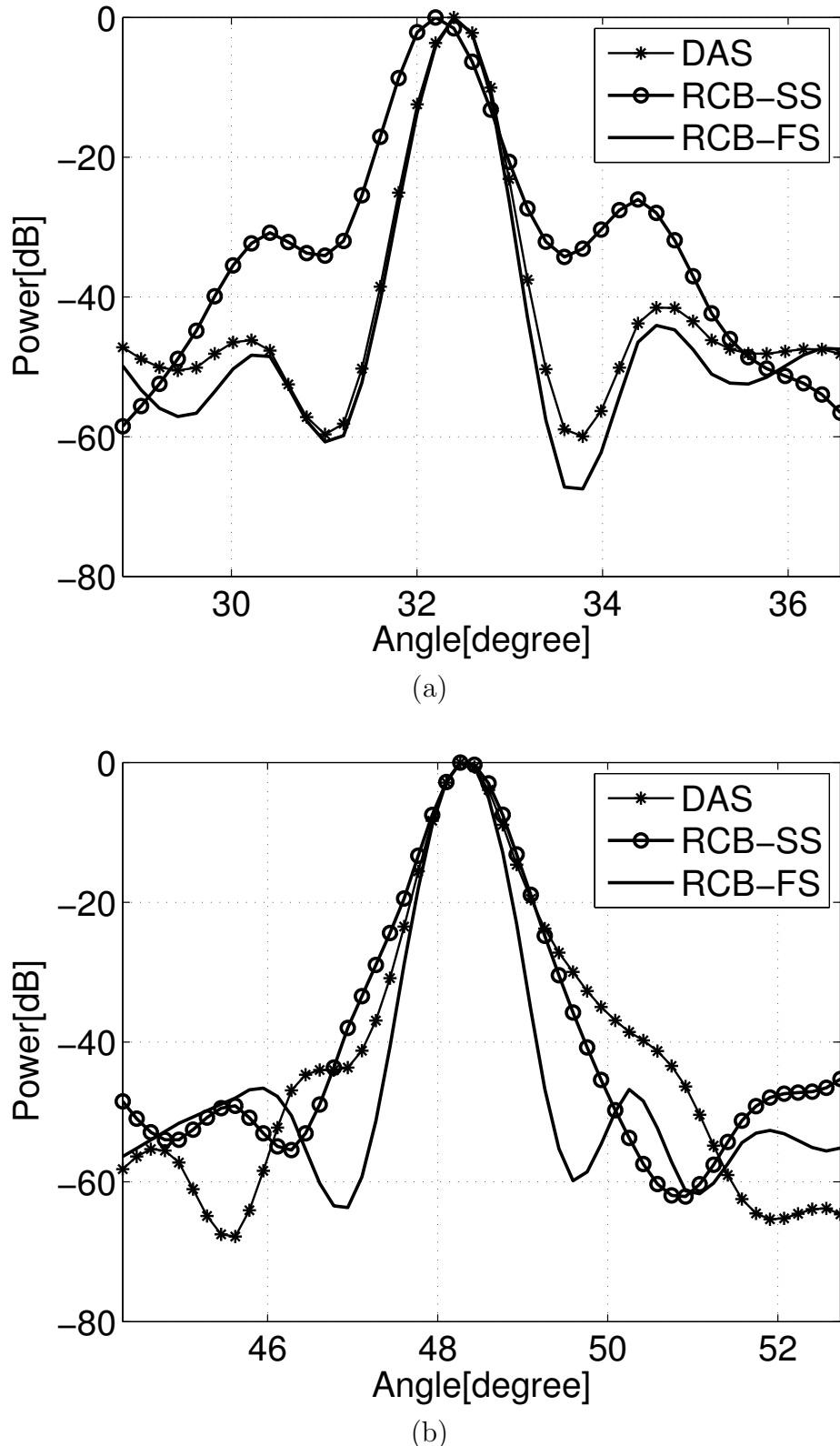


Figure 3.7: Lateral variation of wire targets using the full aperture at depths of (a) 48 mm and (b) 83 mm.

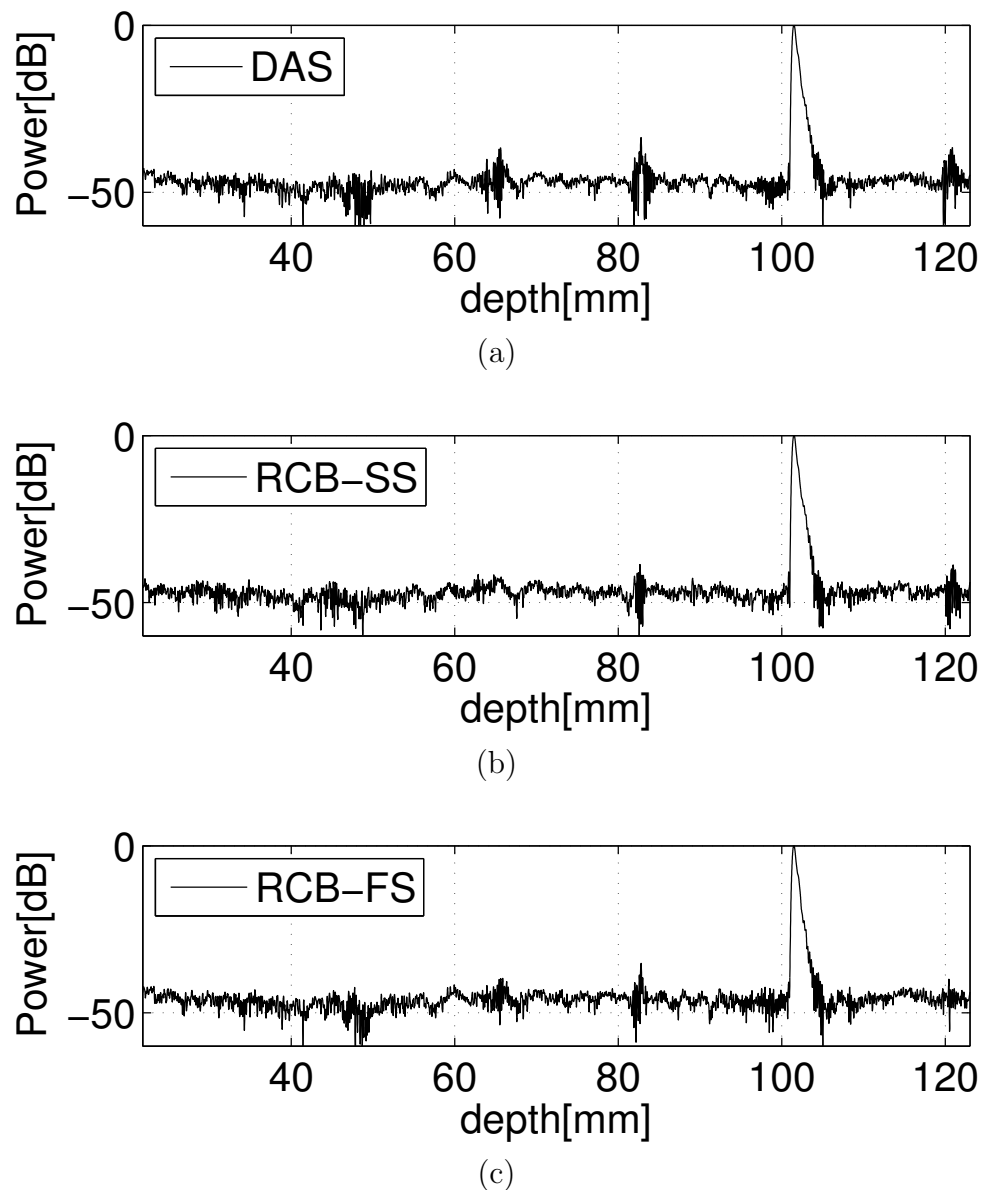


Figure 3.8: Axial variation of wire targets using half the aperture at the 74th scanline (52°) with (a) DAS, (b) RCB-SS and (c) RCB-FS-short.

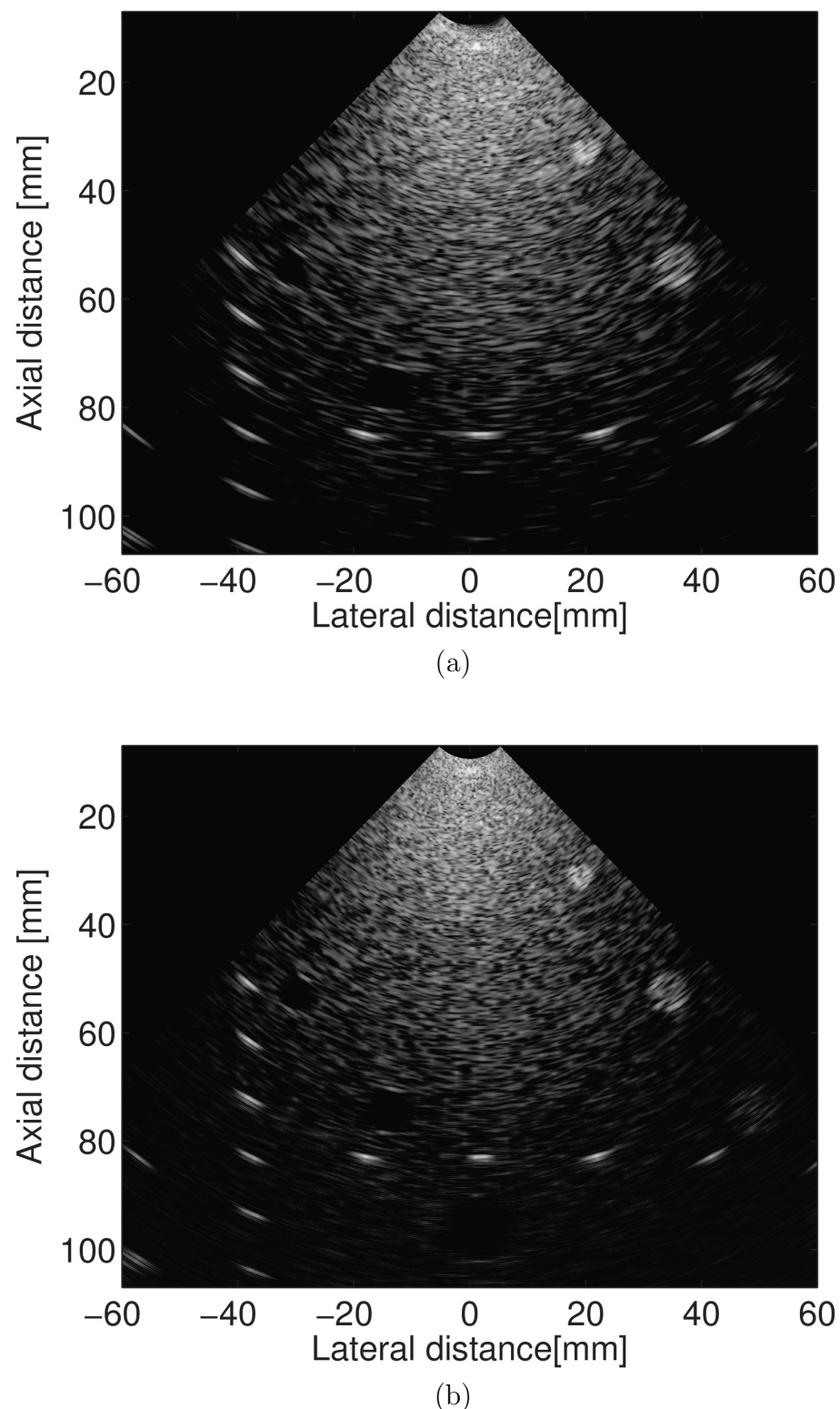


Figure 3.9: Images obtained from experimental data of a *Geabrv* phantom with 64 sensors using (a) RCB-SS and (b) RCB-FS-short.

Chapter 4

RCB-FS with Frequency Compounding

4.1 Introduction

In the last chapter, we demonstrated the improvements on spatial resolution achieved by our proposed robust Capon beamformer with frequency smoothing (RCB-FS). In this chapter, we will demonstrate the performance on speckle reduction of the proposed Capon beamformer with frequency smoothing combined with frequency compounding (RCB-FS-FC). Firstly, we introduce speckle reduction techniques and then propose our speckle reduction approach, robust Capon beamformer with frequency smoothing combined with frequency compounding (RCB-FS-FC).

We first investigate the reconstruction quality of RCB-FS-long, an important implementation step before combining with frequency compounding. We analyze the performance of the RCB-FS-long method using experimental data of wire targets, the heart phantom and the *geab*r phantom from the Biomedical Ultrasonics Laboratory, University of Michigan at Ann Arbor [29]. Our RCB-FS-long method is able to offer us more frequency information for frequency compounding (FC) but first, we need to verify the image quality of the reconstructed image. We implemented fixed focus on transmission and then we applied the aforementioned beamforming algorithms (DAS, RCB-SS, RCB-FS-short and RCB-FS-long) on the data and compared their performances. In spatial smoothing, we chose a sub-aperture width equal to half of the full aperture. The diagonal loading factor was chosen with $\sigma = 1/10$ to get a well conditioned covariance matrix. After the beamforming methods, envelope detection, gain compensation, logarithmic compression and scan conversion were applied.

Then, we investigate the reconstruction quality of RCB-FS-FC using the same

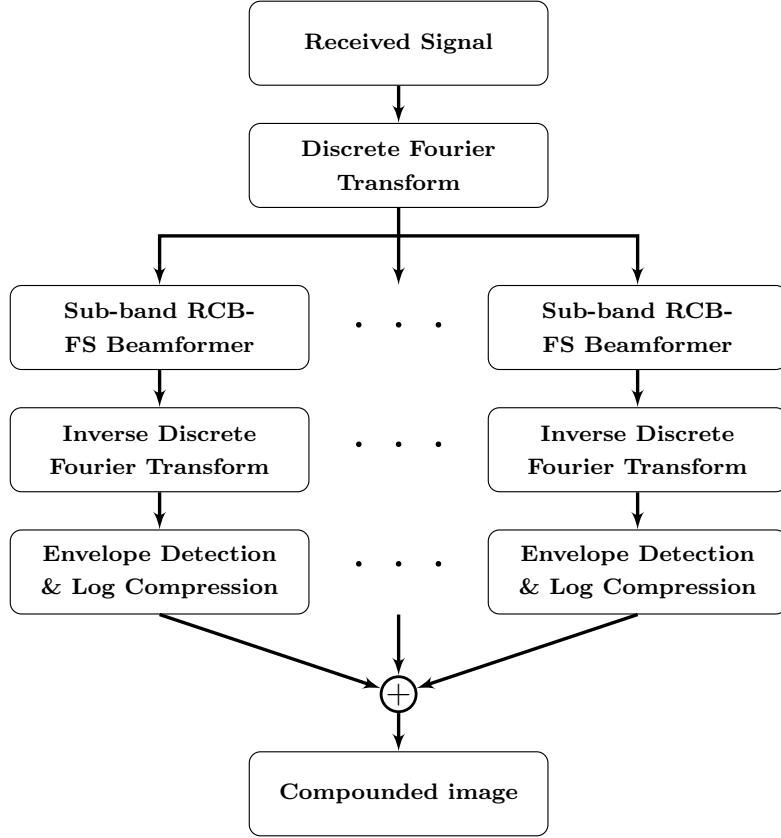


Figure 4.1: Block diagram of RCB-FS-FC.

experimental data of the *gearb* phantom and compare its performance with standard FC. We transform the received time domain signals into the frequency domain and split the spectrum into sub-bands. In standard FC, an inverse discrete Fourier transform is applied to the single sub-bands to form different sub-bands images. In RCB-FS-FC, our proposed frequency domain, adaptive beamforming algorithm was applied to obtain the sub-bands images as shown in Figure 4.1. Envelope detection, gain compensation, logarithmic compression together with scan conversion are applied to each sub-band images separately and then summed to reconstruct the final image. In both experiments, sub-band of half, one-fourth and one-eighth of bandwidth are tested. The overlap of the sub-bands are 0%. The reconstructed images of different sub-band width are evaluated by contrast-to-noise ratio (CNR), speckle signal-to-noise ratio (SNR), histogram pixel intensity (HPI) and edge detection. Furthermore, all the reconstructed images in this paper are displayed over a 45 dB dynamic range.

4.2 Speckle Reduction Techniques

In medical ultrasound imaging, contrast resolution is relatively low and the speckle noise is one of the main artefacts that deteriorate the contrast resolution in the reconstructed images. Speckle comes from the constructive and destructive interferences of the ultrasound wave, which reduces the contrast of the image and obscures the details in reconstructed images [66]. As the interferences depend on the structure of sub-wavelength particles, speckle noise suppression cannot be done by simple averaging. In Figure 4.2, we can see the interference of two reflectors. We can see that the constructive direction θ_c can be found at $\frac{dsin\theta_c}{\lambda} = 0, \pm 1, \pm 2, \dots$, where $\lambda = \frac{c}{f}$ is the wavelength of the wave. The speckle pattern is determined

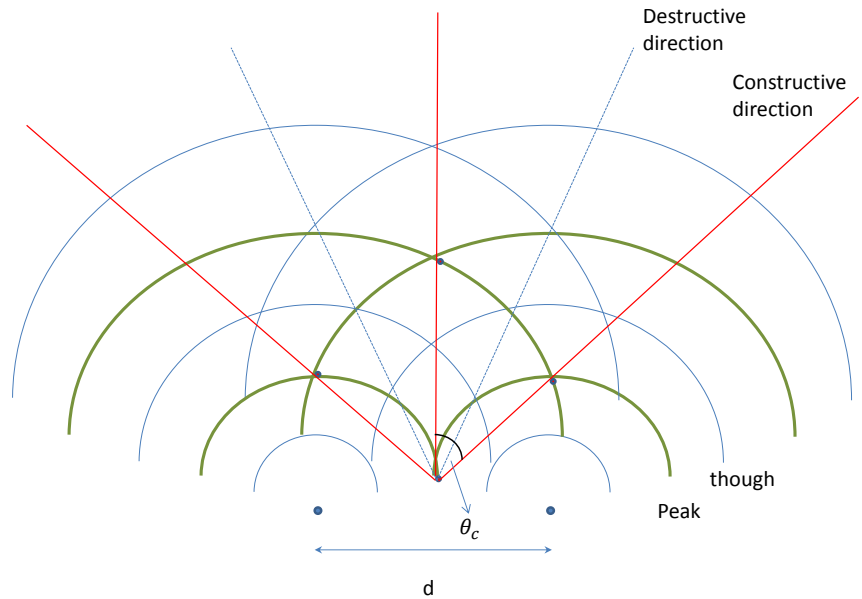


Figure 4.2: The illustration of interference from two point reflectors.

by the frequency and direction of the wave reflected. According to the physics of interference, speckle reduction techniques can be classified into three categories: (i) spatial compounding (SC), (ii) frequency compounding (FC) and (iii) post-filtering. We analyze the performance of the RCB-FS-long method using:

- **Spatial Compounding (SC):** In SC, images with different speckle patterns are formed by sending out pulses with different lateral position or different angles [67, 68]. By averaging these uncorrelated images, the speckle noise will be reduced. The main disadvantage of this method is the loss in lateral resolution due to the use of a short aperture and temporal resolution due

to multiple transmissions. Recently, several researchers have used electronic-beam steering to obtain the images for SC, which overcome some of these tradeoffs [69].

- **Frequency Compounding (FC):**

FC images are formed by compounding different sub-band images. One way of forming these sub-band images is by transmitting different frequency signals sequentially and forming the sub-band images one after another. In this method, the temporal resolution is reduced. Another method to form sub-band images is to divide the spectrum of the received data into sub-bands to form the images. This method is called frequency diversity [70] or split spectrum processing [71]. The drawback of this method is that the axial resolution of the sub-band image is poor due to less frequency information. In recent years, Song *et al.* [72] proposed an adaptive frequency compounding method which finds weights for each sub-band image according to the spectral energy distribution. Sanchez [27] proposed a coded excitation method which enables the increase of bandwidth of the imaging system. Both methods achieve a better contrast and speckle noise reduction but do not improve axial resolution of the images.

- **Post-filtering:** Speckle reducing filters can effectively reduce the speckle without losing the resolution. However, the disadvantage of these filters is that artefacts may be generated. The common speckle filters are Lee, Kuan and Wiener filters. Interested readers can refer to [73, pages 204] for more information.

In order to reduce the speckle noise without sacrificing the axial resolution, we propose a new algorithm by combining the high resolution RCB-FS beamformer with frequency compounding in the next section.

4.3 Proposed Speckle Reduction Method

Frequency compounding is an efficient way to reduce the speckle noise and increase the contrast with a factor of \sqrt{N} between the compounded image and the original one. This factor is hard to achieve by a time domain filter as the sub-band images are usually partial correlated. As RCB-FS performs in frequency domain, we apply a frequency domain filtering and then perform our RCB-FS-FC as shown in Figure 4.1. We first apply the narrowband filtering to the received data, and then form

separate sub-band images by performing envelop detection and log compression. Each sub-band images has its own speckle pattern and the compounded image will cancel out the speckle noise.

In the solution of RCB-FS, we can see that the weights are independent of frequencies. In order to combine RCB-FS with FC, we first divide the bandwidth to N parts and perform RCB-FS for each part. Since RCB-FS requires that the number of sub-bands is no less than the number of transducers M , a long observation time frequency smoothed Capon beamformer, the RCB-FS-long is used to offer more available sub-bands. For frequency group n , we have the frequency in the interval $k - [k_nl, k_nh]$ and the optimized weights are given by,

$$\mathbf{w}_n(\mathbf{r}) = \frac{(\bar{\mathbf{R}}_n(\mathbf{r}) + \epsilon_n \mathbf{I}_n)^{-1} \mathbf{a}_n(\mathbf{r})}{\mathbf{a}_n(\mathbf{r})^H (\bar{\mathbf{R}}_n(\mathbf{r}) + \epsilon_n \mathbf{I}_n)^{-1} \mathbf{a}_n(\mathbf{r})}, \quad (4.1)$$

where $\bar{\mathbf{R}}_n(\mathbf{r}) = \frac{1}{K} \sum_{k=k_nl}^{k_nh} \mathbf{R}(k, \mathbf{r}) \Delta \omega_n$. ϵ_n is the diagonal loading factor which will be optimized by experimental data. Then, we can find the optimized sub-band beamformed output for RCB-FS-FC as

$$y_n(\mathbf{r}) = \sum_{k=k_nl}^{k_nh} \mathbf{w}_n(\mathbf{r})^* \mathbf{X}_n(k, \mathbf{r}) \quad (4.2)$$

Thereafter, envelop detection and log compression are applied to form a high resolution sub-band image. For different frequency sub-band images, the speckle patterns are different. Typically, by summation of N independent sub-band images, the speckle statistics will be reduced approximately to \sqrt{N} [66]. Therefore, FC is an important extension to RCB-FS.

In order to have enough number of sub-bands, more time domain samples are required. This can be done by longer observation time or interpolation. In this paper, a longer observation time is used so as to minimize artefact from interpolation. A long observation time can increase the robustness of the beamformer as the independently distributed noise is increased and cancelled out. As the covariance matrix is pre-steered to the point of interest, the signals along the axial distance will be treated as off-axis signals and will be minimized by the beamformer.

4.4 Evaluation Metrics

To evaluate the performance of the speckle reduction of the resulting ultrasound image, the following metrics were used in this chapter.

Contrast-to-noise Ratio (CNR)

CNR [74] is one of the quantitative measurements to assess the contrast between the area of interest and the background tissue; it is also known as contrast-to-speckle ratio, which is defined as

$$CNR = \left| \frac{\mu_B - \mu_S}{\sqrt{\sigma_B^2 + \sigma_S^2}} \right| \quad (4.3)$$

where μ_B and μ_S are the mean value of the background and the place of interest, σ_B^2 and σ_S^2 are the variance of the background and the place of interest. CNR is an important metric to evaluate the ability to extract the area of interest from the background.

Signal-to-noise ratio (SNR)

SNR is one of the quantitative measurements to assess the speckle fluctuations in a particular region, which is also known as speckle signal-to-noise ratio. The SNR is defined as

$$SNR = \frac{\mu_S}{\sigma_S} \quad (4.4)$$

In theory, the SNR in a Rayleigh scatter model is 1.91 and a \sqrt{N} improvement can be achieved by compounding N independent images [66].

Histogram pixel intensity (HPI)

HPI describes the distribution of gray-scale pixel intensities in an image. In ultrasound imaging, the HPI of the target and the background are plotted separately. The percentage of overlap, histogram overlap (HO), describes the detectability of the target.

Edge detection

Edge detection is the image of boundaries. Usually, boundaries are the curve of rapid change in image intensity. The quality of the boundaries determine the detectability of the target.

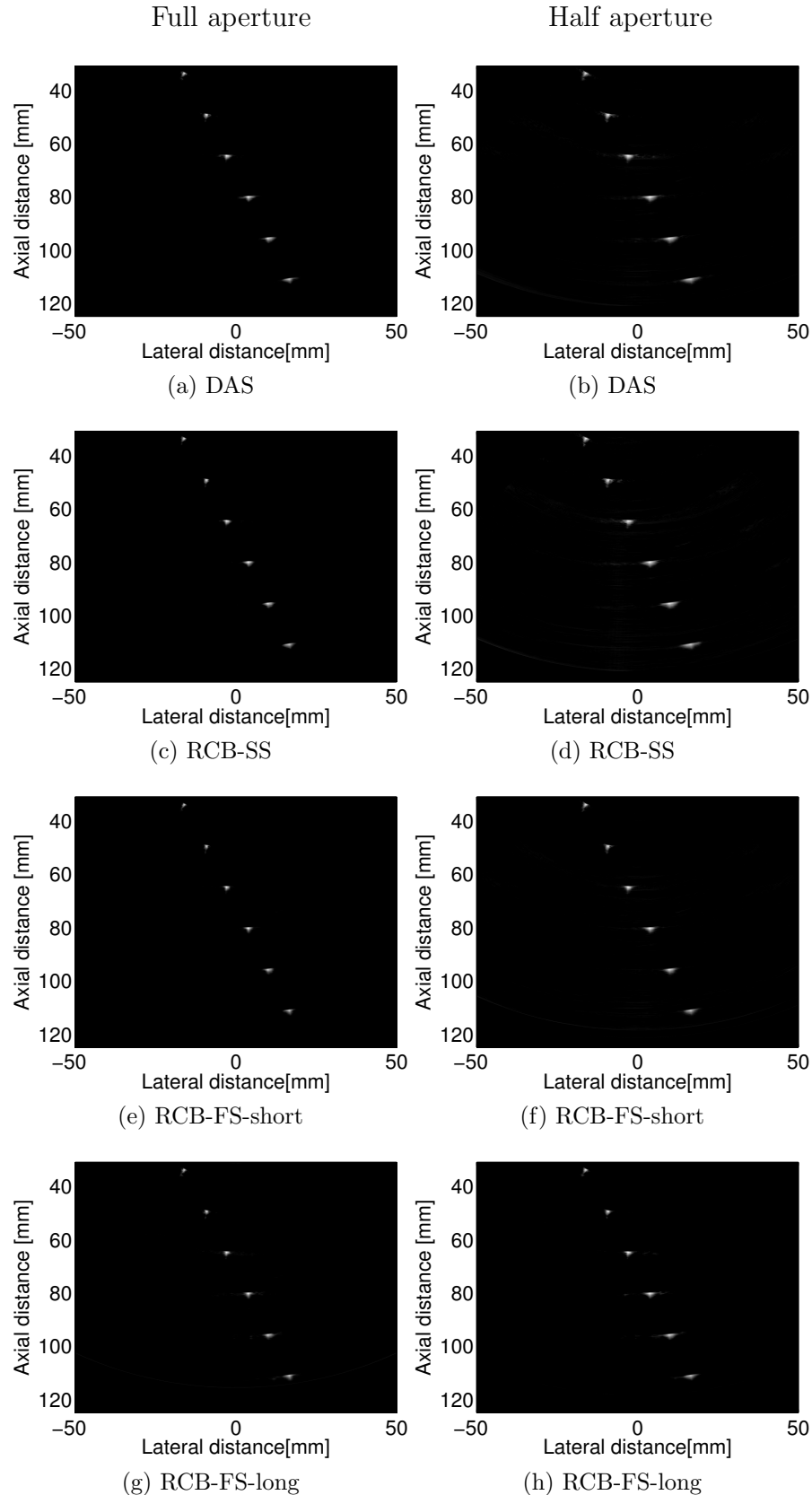


Figure 4.3: Images obtained from experimental data of wire targets: left: (a) DAS, (c) RCB-SS and (e) RCB-FS-short, (g) RCB-FS-long using full aperture; right: (b) DAS, (d) RCB-SS, (f) RCB-FS-short and (h) RCB-FS-long using half aperture.

Method	Element	FWHM (deg.)	PSL (dB)
DAS	128	0.98	- 46
RCB-SS	128	0.91	- 46
RCB-FS-short	128	0.56	- 50
RCB-FS-long	128	0.57	- 50
DAS	64	1.75	- 40
RCB-SS	64	1.68	- 41
RCB-FS-short	64	1.05	- 46
RCB-FS-long	64	1.09	- 45

* The Rayleigh resolution limit for 128 elements is 0.86 degree.

* The Rayleigh resolution limit for 64 elements is 1.72 degree.

Table 4.1: Average FWHM and PSL of different algorithms

4.5 RCB-FS with Long Observation Time

4.5.1 Wire Targets

We applied the three methods on experimental data for six wire targets to compare the resolution between DAS, RCB-SS, RCB-FS-short and RCB-FS-long. The wires were placed at axial distances of 34, 48, 65, 83, 101 and 121 mm. The ultrasound data was collected by 128 transducers with central frequency 3.5 MHz, and sampled at 13.8889 MHz.

For the first set of reconstructions, we used the full aperture (128 transducers) to transmit and receive. The ultrasound images reconstructed using the full aperture are shown in Figure 3.6 (a), (b), (c) and (d).

We observed that the size of wire targets in RCB-FS-long is smaller than those in RCB-SS and DAS. Moreover, we can see that the performance between RCB-FS-short and RCB-FS-long is similar, which enables further implementations for sub-band frequency compounding.

The lateral resolution of RCB-FS with long observation time is similar to the short observation time as shown in Table 4.1 quantitatively.

We compared the axial variation of the three methods with half aperture at 52° (74th scanline), see Fig 4.4. Here, the RCB-FS with long observation time cannot suppress the interferences as much as RCB-SS and RCB-FS-short but performs better than DAS.

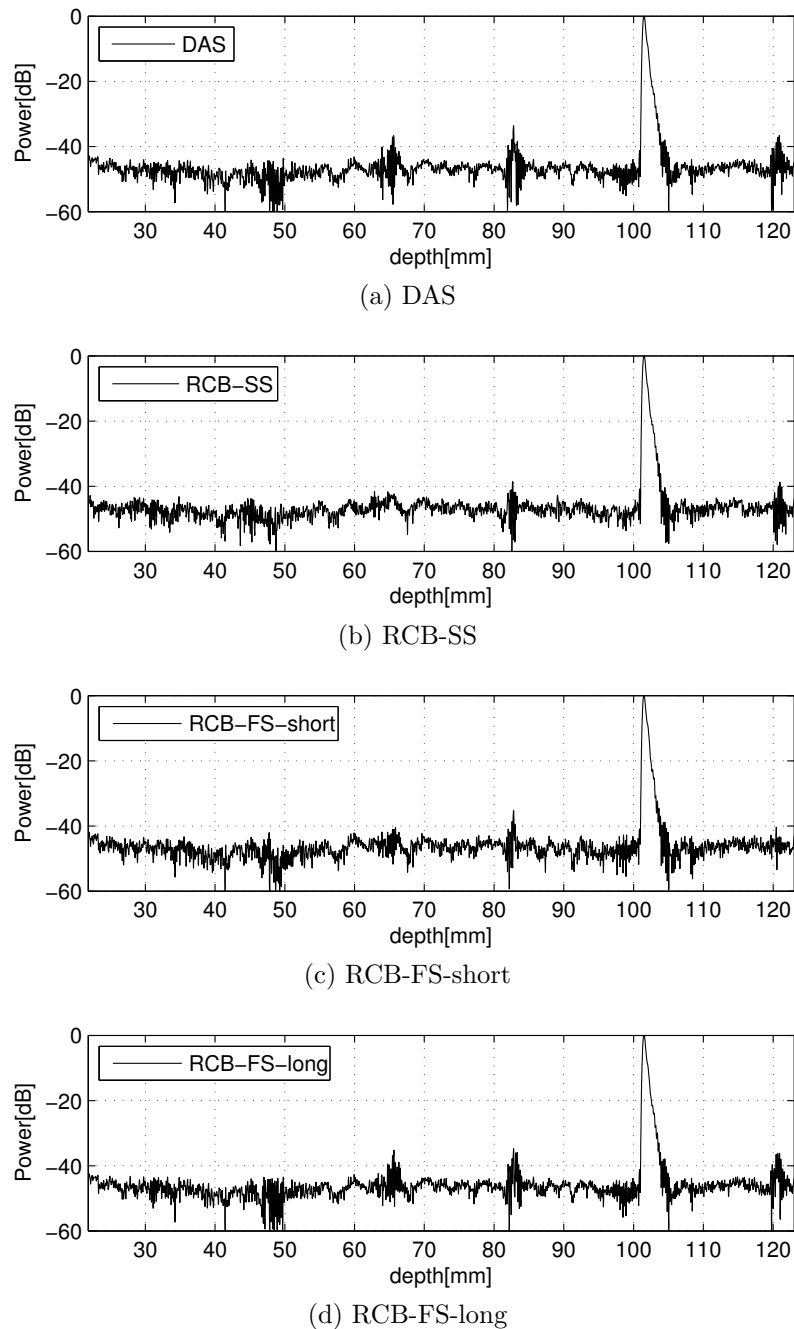


Figure 4.4: Axial variation of wire targets using half the aperture at the 74th scanline (52°) with (a) DAS, (b) RCB-SS, (c) RCB-FS-short and (d) RCB-FS-long.

4.5.2 Phantoms

We applied our algorithm on experimental data of a heart phantom and a *geabr* phantom. The better performance of RCB-SS over that of DAS is illustrated in [75]. Here, we only compared the image quality between RCB-SS, RCB-FS-short and RCB-FS-long. The image data was collected by 64 transducers with central frequency 3.333 MHz, at 17.76 MHz sampling frequency. The reconstructed images are shown in Figure 4.5.

We focused on the area circled to analyze the speckle statistics between the two algorithms. The speckle size in RCB-FS is smaller than that in RCB-SS. This smaller size of speckle means a better definition on the object boundaries. The SNR of Heart phantom of RCB-SS is 1.87 ± 0.01 while SNR in RCB-FS is 2.21 ± 0.01 which shows less speckle fluctuation in the heart phantom for RCB-FS method. SNR of the lesion in the *geabr* phantom of RCB-SS is 1.65 ± 0.01 while SNR in RCB-FS is 2.67 ± 0.01 which also shows less speckle fluctuation for the proposed method. When edge detection is applied to the lesion in the red circle of the *geabr* phantom, we can see better detectability of the lesion and a more constant distribution within the boundary as shown in Figure 4.6.

The lateral resolution of the proposed RCB-FS-long is better than that of DAS and RCB-SS quantified in the wire target experiment. The improvement against DAS comes from the super-resolution adaptive Capon beamformer. The FWHM of RCB-FS is smaller than Rayleigh resolution limit. Compared to RCB-SS, a better resolution in RCB-FS-long comes from a fact that the effective aperture size is doubled. The possibility of reducing the aperture while keeping a good image quality enables a reduction on the data storage memory and computational complexity and increase temporal resolution. In this dissertation, we trade this better resolution to reduce the speckle noise in ultrasound images and propose a RCB-FS-FC method.

4.6 RCB-FS-FC

4.6.1 Overall Image Quality

From the results above, the image quality of RCB-FS-long is good compared to other beamformer like DAS and RCB-SS. To further reduce the speckle, RCB-FS-FC was proposed. In this section, the half-, one-fourth-, one-eighth- sub-band width RCB-FS-FC were tested and compared to standard FC with the same sub-band widths. The overall performance of the reconstructed images are shown in

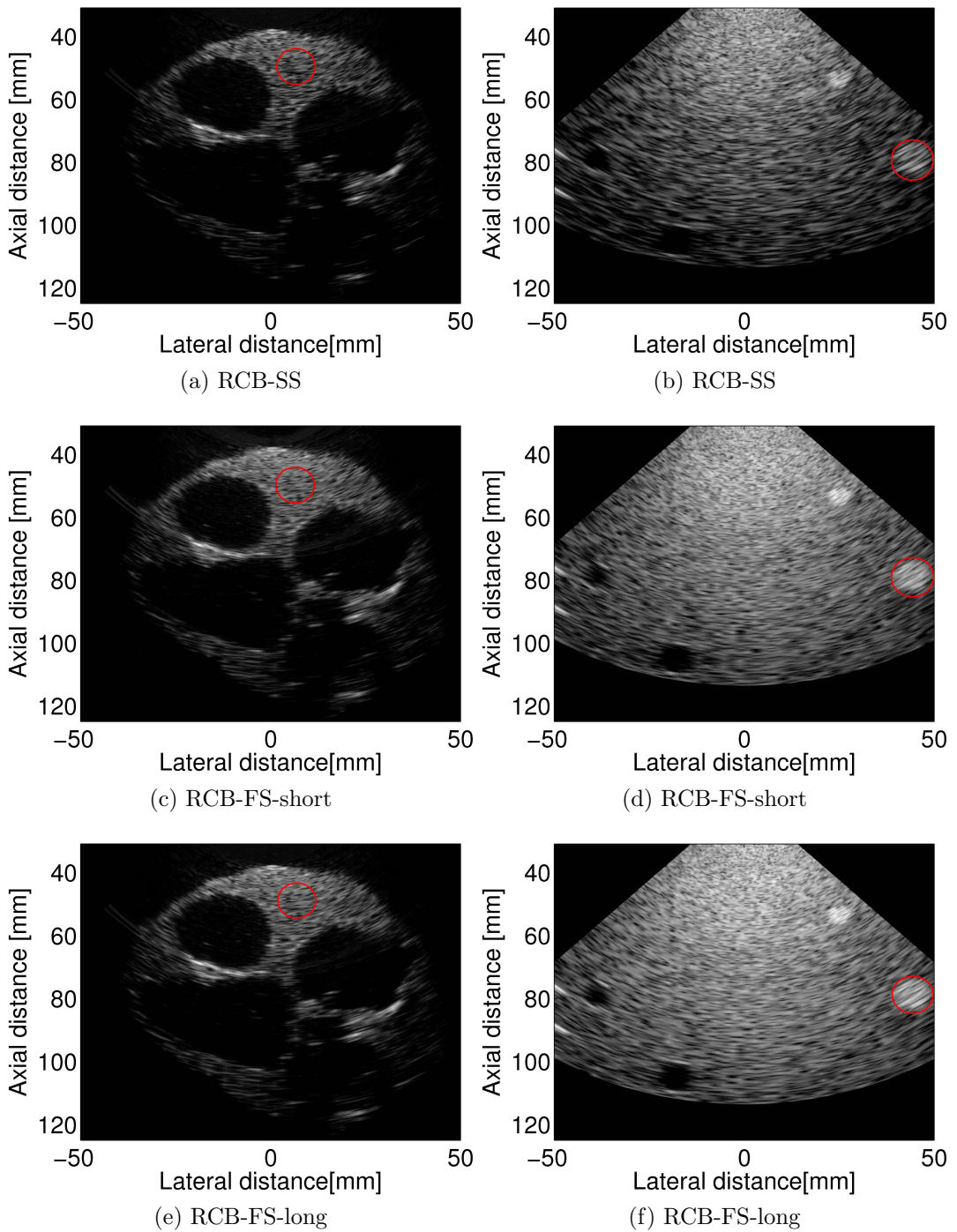


Figure 4.5: Images obtained from heart phantoms: using (a) RCB-SS, (c) RCB-FS-short and (e) RCB-FS-long and *geab* phantoms: using (b) RCB-SS, (d) RCB-FS-short and (f) RCB-FS-long.

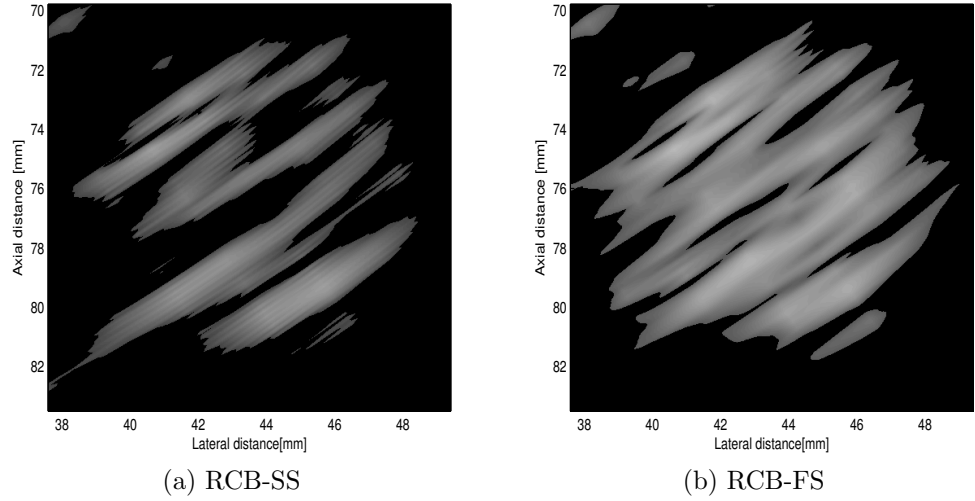


Figure 4.6: Edge detection of lesion in *gearb* phantoms using: (a) RCB-SS and (b) RCB-FS.

Figure 4.7. For the half bandwidth case, it can be seen that the two dark areas are hard to be seen in the FC image while they are clear in the RCB-FS-FC. Moreover, the resolution at the higher depth is higher in the RCB-FS-FC image. In addition, the boundaries of lesions in RCB-FS-FC is finer defined. In the half-width case, we can see that some distortions of image in the axial direction happen in the FC image but when RCB-FS-FC is applied, the reconstructed image still keeps a good axial resolution. In the one-fourth width case, the speckle is significantly reduced in the reconstructed image but at the expense of slightly blurring the image. The dark lesion can still be seen in the RCB-FS-FC case but the contrast is low. For the one-eighth width case, the resolution in both images are in low condition; however, it is not hard to see a better contrast and resolution and finer boundary in RCB-FS-FC. The better performance comes from optimal weights for each sub-band reconstructed images as shown in Figure 4.8. This figure shows the reconstructed sub-band images for the one-fourth bandwidth case. It can be seen that a better resolution and contrast is achieved by using the RCB-FS beamforming. We can see that the boundaries of lesions are clearly defined. In addition, the two dark lesions at the left side of image are not visible in the sub-band image of FC, which is the reason why they are not visible in the final compounding image.

4.6.2 Analysis

To analyse the speckle statistics quantitatively, we focus on the same lesion area as chosen in Figure 4.5. We calculated the CNR and SNR in the central part of the le-

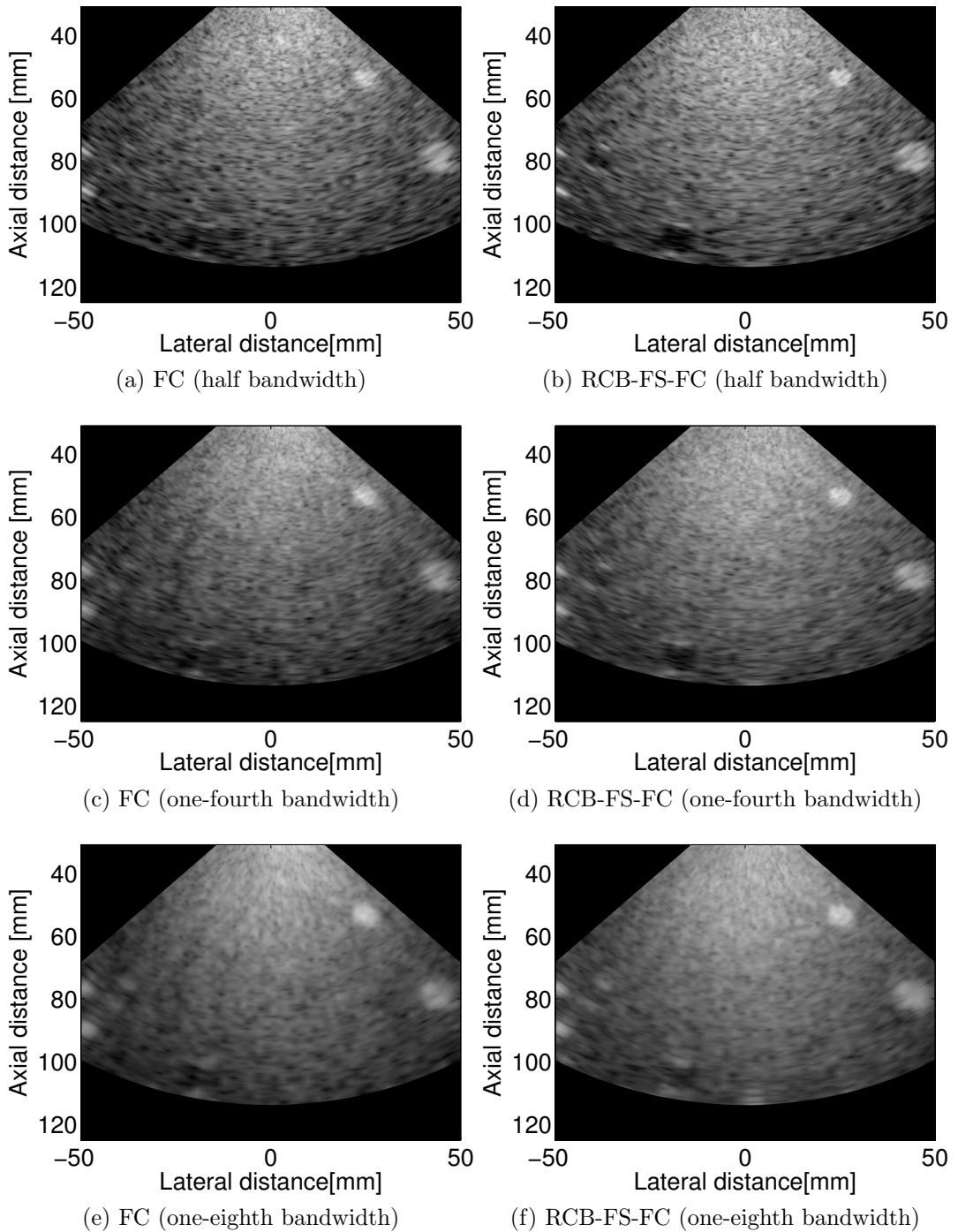


Figure 4.7: Compounded B-mode Images: obtained from *gearbr* phantom using: (a) FC with half bandwidth, (b) RCB-FS-FC with half bandwidth, (c) FC with one-fourth bandwidth, (d) RCB-FS-FC with one-fourth bandwidth, (e) FC with one-eighth bandwidth and (f) RCB-FS-FC with one-eighth bandwidth.

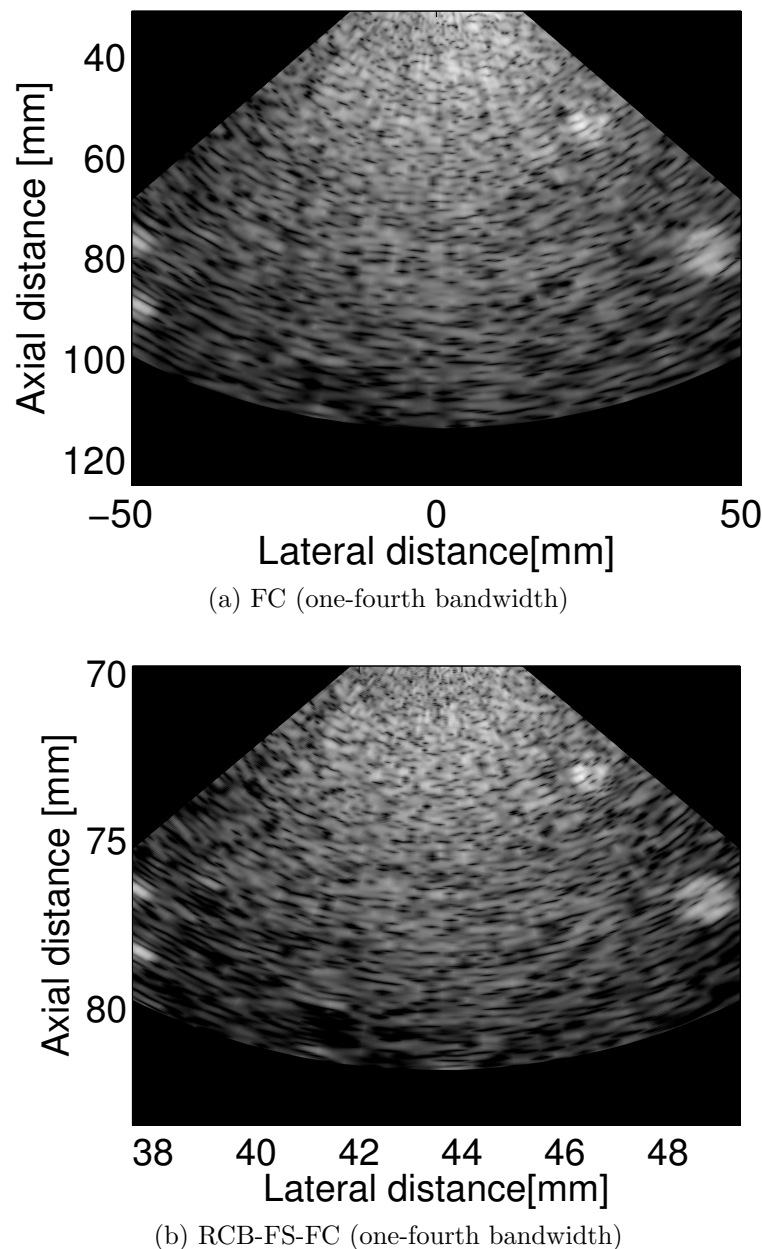


Figure 4.8: Sub-band B-mode Images: obtained from *geabrv* phantom using: (a) FC with one-fourth bandwidth and (b) RCB-FS-FC with one-fourth bandwidth.

sion. In Table 4.2, CNR and SNR results are summarized for the three cases. From

Table 4.2: Speckle Statistics

Method	Bandwidth	CNR	SNR	HO
FC	Half	1.36	2.70	18%
RCB-FS-FC	Half	1.40	2.81	17%
FC	One-fourth	1.54	2.83	4%
RCB-FS-FC	One-fourth	1.66	3.14	2%
FC	One-eighth	1.68	3.40	1%
RCB-FS-FC	One-eighth	1.79	3.78	0%

the table, the CNR and SNR is increased as the sub-band images are increased, which means a higher contrast and lower speckle noise can be achieved by frequency compounding. When using the RCB-FS weights, the CNR and SNR are improved. The amount of improvement in CNR and SNR for half-width case is around 3%. As the more sub-band images are used, the CNR and SNR improvement is increased to around 10%.

Histograms of the background and target regions are shown in Figure 4.9. In the half-width case, there is a large overlap between the background and the lesion of interest, which is because there is a large standard deviation or speckle in the image. As the more sub-band images are used, the overlap is reduced from 18% to nearly no overlap. In addition, we can see the overlap in RCB-FS-FC is less than that in FC. In the RCB-FS-FC, an ideal status of zero overlap is achieved by compounding eight sub-band images.

Then, we applied the edge detection on all the reconstructed images and obtained Figure 4.10. From the figures, the axial resolution (northwest direction) is much better in the RCB-FS-FC. In the half-width case, the background and the lesion is not separated well enough in both reconstructed images. However, the lesion begins to distort in axial direction for FC. In the eighth-width case, both reconstructed images have been extracted from the background; however, we can see a circular shape is still kept in RCB-FS-FC while the image is distorted in the FC case.

4.7 Discussions

In this chapter, we verified another RCB-FS implementation, RCB-FS-long on medical ultrasound imaging. RCB-long can offer us more frequency sub-bands for use in frequency compounding. RCB-FS-long achieves a similar performance with

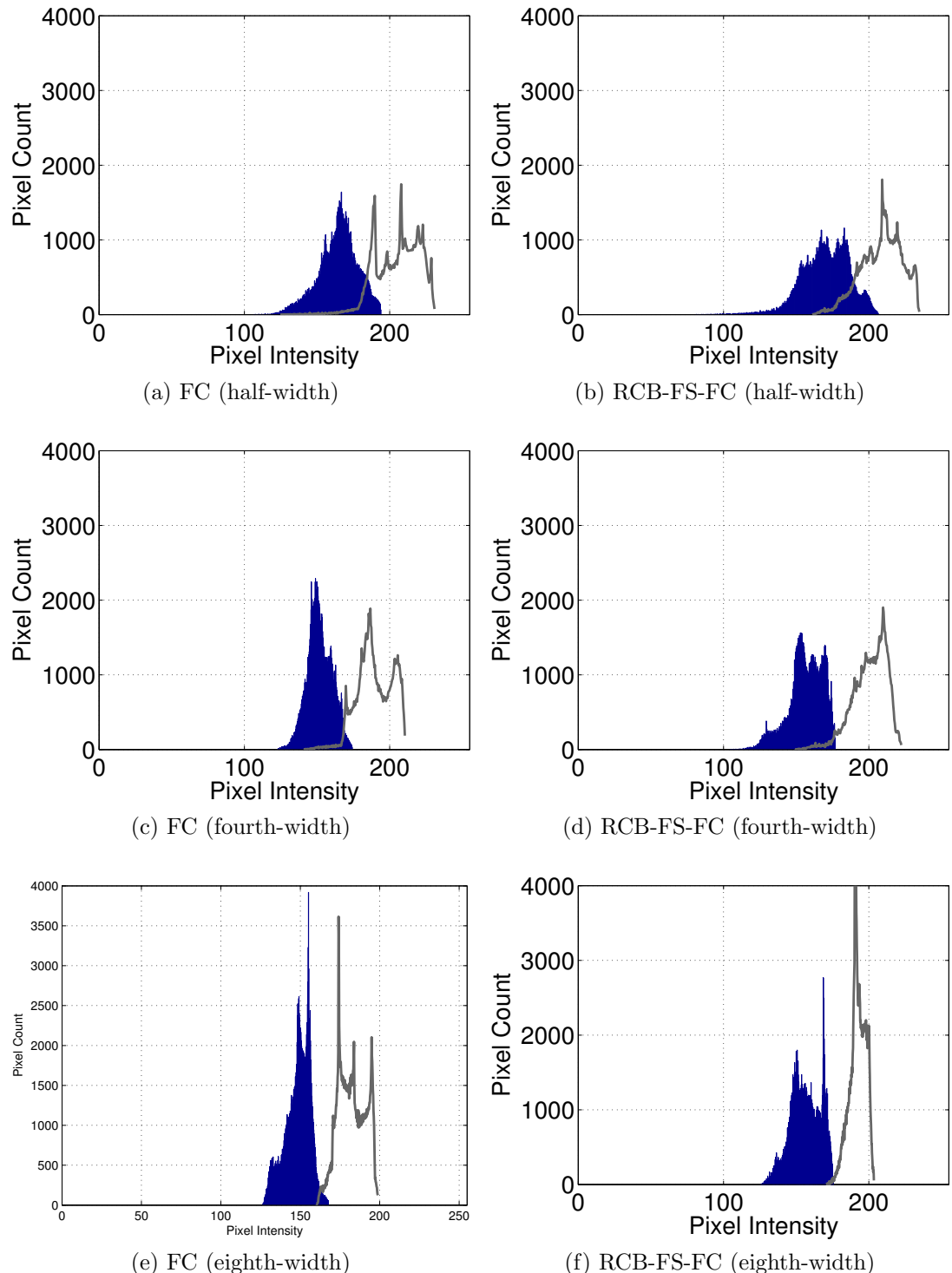


Figure 4.9: Histogram for *gearb* phantom: (a) FC with half-width, (b) RCB-FS-FC with half-width, (c) FC with fourth-width, (d) RCB-FS-FC with fourth-width, (e) FC with eighth-width and (f) RCB-FS-FC with eighth-width.

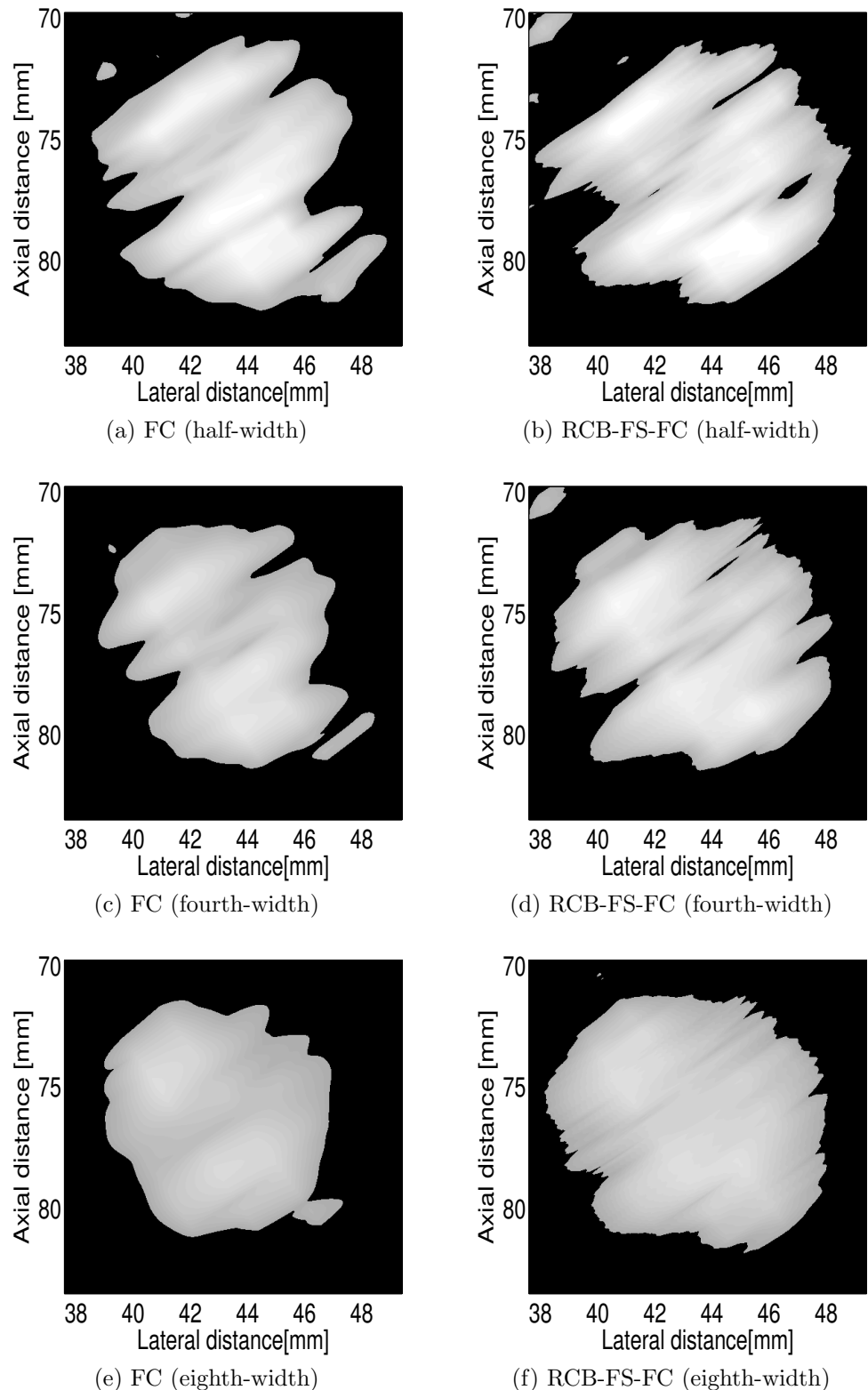


Figure 4.10: Edge detection of lesion (bright circle region) in *geabR* phantom: (a) FC with half-width, (b) RCB-FS-FC with half-width, (c) FC with fourth-width, (d) RCB-FS-FC with fourth-width, (e) FC with eighth-width and (f) RCB-FS-FC with eighth-width.

RCB-FS-short but still better than RCB-SS and DAS. However, the axial resolution is worse than both RCB-SS and RCB-FS.

In RCB-FS-FC, we can see obvious improvements on image quality compared to standard FC method. The most important finding is that axial distortions in RCB-FS-FC images are small while the speckle reduction is better. A better speckle reduction can be done by coded excitation [27], and that is easy to combine with RCB-FS as well. All the results show better detectability for RCB-FS-FC than FC. In addition, among all the cases, in RCB-FS-FC, as the number of sub-band reconstructed images increases, the speckle noise keeps reducing and the contrast keeps increasing, at the expense of lowering the resolution and blurring the image. In the half-width case, the reconstructed image with RCB-FS-FC keeps all the information in the phantom with a better contrast and a high speckle signal to noise ratio of 2.81 which is 47% higher than rayleigh distributed noise. Eighth-width case using RCB-FS-FC shows a nearly ideal separation from the background and a perfect shape detection - similar to a circle shape. For fourth-width case, using RCB-FS-FC method, a good resolution, low speckle noise image is obtained, which is the optimal condition for reconstructing the image.

4.8 Summary

In this chapter, we examine a new implementation of RCB-FS, RCB-FS-long. RCB-FS-long performs well enough for further combination with the frequency compounding (FC) method.

After verifying the performance of RCB-FS-long, we applied the proposed frequency smoothed robust Capon beamformer with frequency compounding on the *geabr* phantom data. Particular focus has been put on the lesion area and qualitative analysis on the contrast and speckle of the image generated has been carried out. Compared to standard FC, our method obtains a higher SNR and CNR ratio. More of the lesion information can be seen in the reconstructed image for the proposed method. In addition, our compounding method shows a significant improvement in resolution and better detection of the lesion boundaries. We verify the performance of the proposed RCB-FS-FC method which offers a better image reconstruction on speckle reduction.

Chapter 5

Conclusions and Future Work

5.1 Conclusions

In this dissertation, we proposed a new adaptive beamforming method RCB-FS for finding the optimal weights for ultrasound imaging. In recent years, Robust Capon Beamformer with Spatial Smoothing (RCB-SS) has improved ultrasound imaging. However, the RCB-SS is implemented in the time domain and spatial smoothing has the disadvantage of reducing the effective aperture leading to lower lateral resolution.

Compared to the existing methods, our method is implemented in the frequency domain which utilizes the large bandwidth to suppress off-axis interference. In addition, the frequency smoothing method decorrelates the signal covariance matrix without any deterioration on image quality. We evaluated the proposed method using FWHM and PSL and compared the performance with DAS and RCB-SS. Our method showed better performance. In addition, the RCB-FS has good performance even with small apertures allowing lower data storage, smaller computational complexity and higher temporal resolution.

In order to further reduce the speckle noise, we proposed a RCB-FS-FC method to combine our proposed method and FC. In order to obtain more available subbands for use in FC, we first proposed an RCB-FS-long method and evaluated its performance. The performance of RCB-FS-long is similar to RCB-FS-short in terms of FWHM and PSL. The axial resolution of RCB-FS-long is worse than RCB-FS and RCB-SS but still better than DAS.

After evaluating the RCB-FS-long method, we examined the proposed RCB-FS-FC method using a phantom with lesions. Compared to standard FC, our method obtains a higher SNR and CNR ratio while maintaining most of the lesion information in the reconstructed image. In addition, our compounding method

shows better resolution, sharper boundaries and finer detection of lesions. In the eighth-width case, a nearly ideal separation between the lesion and the background is achieved. RCB-FS-FC offers a new way to optimize the sub-band reconstructed image and achieves significant improvement on image quality.

5.2 Future Work

In this section, we outline a number of future research directions that arise from the work presented in this thesis.

RCB-FS applied to ultrafast imaging: In this dissertation, the proposed RCB-FS method is applied to focused data and achieves improvements in image quality. However, in ultrafast imaging, the image quality is sacrificed for high frame rate imaging. It is of great benefit to investigate the proposed high resolution beamformer to ultrafast imaging. This may improve the temporal resolution of the medical ultrasound imaging systems without sacrificing the spatial resolution.

RCB-FS applied to harmonic imaging: Harmonic imaging is different from conventional imaging as it is generated during the propagation of the transmitted pulse. Harmonic imaging can minimize artefacts in ultrasound imaging but the resolution is low due to the low signal-to-noise ratio. Applying the proposed high resolution frequency domain beamformer to harmonic imaging may further utilise the frequency information and achieve a better image quality.

RCB-FS applied to 3D ultrasound imaging: 3D or even 4D imaging is an important research area in ultrasound imaging. In this dissertation, a linear array beamforming method was applied to B-mode images to improve the image quality. It is of great value to implement the method using a 2D array and apply it to the 3D imaging.

Implementation of RCB-FS-FC method: In this dissertation, although the resolution and shape of the lesion is improved significantly, the CNR and SNR of the proposed RCB-FS-FC is not improved a lot compared to the FC method. The coded excitation method is especially good at improving the CNR and SNR in frequency compounding (FC) [27]. As a result, it will be important to try combining the two methods. In addition, in the RCB-FS-FC method, we found the optimized weights for each transducer to obtain a good sub-band image but in

forming final image by summing the sub band images, we did not apply adaptive weightings in this sum. Each sub band image was given equal weighting. It is worthwhile to investigate an adaptive weight to this sum of sub band images. This could result in better speckle reduction while minimizing the loss the resolution even further.

References

- [1] “Compare and contrast MRI, CT Scan and Ultrasound,” http://www.cyberphysics.co.uk/topics/medical/compareMRI_CT_US.htm, accessed “May., 2014”.
- [2] S. H. C. Ortiz, T. Chiu, and M. D. Fox, “Ultrasound image enhancement: A review,” *Biomedical Signal Processing and Control*, vol. 7, no. 5, pp. 419–428, Sep. 2012.
- [3] P. R. Hoskins, K. Martin, and A. Thrush, *Diagnostic Ultrasound: physics and equipment*. NY, USA: Cambridge University Press, 2010.
- [4] W. R. Hedrick, D. L. Hykes, and D. E. Starchman, *Ultrasound Physics and instrumentation*. St. Louis, Missouri, USA: Elsevier Mosby Press, 2005.
- [5] K. K. Shung, J. Cannata, Q. Zhou, and J. Lee, “High frequency ultrasound: a new frontier for ultrasound,” in *31st International Conference of the IEEE EMBS*, Minnesota, USA, Sep. 2009, pp. 1953–1955.
- [6] M. Ibnkahla, *Adaptive signal processing in wireless communications*. Boca Raton, FL, USA: CRC Press, 2009.
- [7] J. A. Mann and W. F. Walker, “A constrained adaptive beamformer for medical ultrasound: initial results,” in *Ultrasonics Symposium, 2002 IEEE*, vol. 2, Munich, Germany, Oct. 2002, pp. 8–11.
- [8] M. Sasso and C. C. Bacrie, “Medical ultrasound imaging using the fully adaptive beamformer,” in *IEEE International Conference on Acoustics, Speech, and Signal Processing*, vol. 2, Philadelphia, Pennsylvania, USA, Mar. 2005, pp. 489–492.
- [9] S. Khezerloo and D. Rakhmatov, “Gradient-driven beamforming for biomedical ultrasound,” in *Conferernce of IEEE Engineering in Medicine and Biology Society*, Victoria, British Columbia, Canada, Dec. 2009, pp. 444–450.

- [10] J. F. Synnevåg, A. A. Nilsen, and S. Holm, “Adaptive beamforming applied to medical ultrasound imaging,” *IEEE Trans. on Ultrasonics, Ferroelectrics, and Frequency Control*, vol. 54, no. 8, pp. 1606–1613, Aug. 2007.
- [11] F. Vignon and M. R. Burcher, “Capon beamforming in medical ultrasound imaging with focused beams,” *IEEE Trans. on Ultrasonics, Ferroelectrics, and Frequency Control*, vol. 55, no. 3, pp. 619–628, Mar. 2008.
- [12] A. C. Jensen and A. Austeng, “An approach to multibeam covariance matrices for adaptive beamforming in ultrasonography,” *IEEE Trans. on Ultrasonics, Ferroelectrics, and Frequency Control*, vol. 59, no. 6, pp. 1139–1148, June 2012.
- [13] S. Mehdizadeh, A. Austeng, T. F. Johansen, and S. Holm, “Eigenspace based minimum variance beamforming applied to ultrasound imaging of acoustically hard tissues,” *IEEE Trans. on Medical Imaging*, vol. 31, no. 10, pp. 1912–1921, Oct. 2012.
- [14] I. K. Holfort, F. Gran, and J. A. Jensen, “Minimum variance beamforming for high frame-rate ultrasound imaging,” in *IEEE Ultrasonics Symposium*, New York, USA, Oct. 2007, pp. 1541–1544.
- [15] A. C. Kak and M. Slaney, *Principles of Computerized Tomographic Imaging*. New York, USA: IEEE Press, 2001.
- [16] B. Glen, *Handbook for sound engineer*. NJ, USA: Focal Press, 2005.
- [17] E. C. Jordon and K. G. Balmain, *Electromagnetic waves and radiating systems*. NJ, USA: Prentice Hall, 1968.
- [18] D. H. Johnson and D. E. Dudgeon, *Array Signal processing: concepts and techniques*. NJ, USA: Prentice Hall, 1993.
- [19] D. A. Naylor and M. K. Tahic, “Apodizing functions for fourier transform spectroscopy,” *J. Opt. Soc. Am.*, vol. 24, no. 11, pp. 3644–3648, Nov. 2007.
- [20] J. Capon, “High-resolution frequency-wavenumber spectrum analysis,” *Proceedings of the IEEE*, vol. 57, no. 8, pp. 947–949, Aug. 1969.
- [21] Y. Fathi, A. Mahloojifar, and B. M. Asl, “GPU-based adaptive beamformer for medical ultrasound imaging,” in *Iranian Conference on Biomedical Engineering, 2012*, Tehran, Iran, Dec. 2012, pp. 113–117.

- [22] Z. Wang, J. Li, and R. Wu, "Time-delay- and time-reversal-based robust Capon beamformers for ultrasound imaging," *IEEE Trans. on Medical Imaging*, vol. 24, no. 10, pp. 1308–1322, Oct. 2005.
- [23] B. M. Asl and A. M. Maholoojifar, "Contrast enhancement and robustness improvement of adaptive ultrasound imaging using forward-backward minimum variance beamforming," *IEEE Tran. on Ultrasonics, Ferroelectrics, and Frequency control*, vol. 58, no. 4, pp. 858–867, Apr. 2011.
- [24] D. A. Linebarger and D. H. Johnson, "The effects of spatial averaging on coherence and resolution," *IEEE Tran. on Acoustics, Speech, and Signal Processing*, vol. 38, no. 5, pp. 2865–2868, May 1990.
- [25] J. G. Abbott and F. L. Thurstone, "Acoustic speckle: Theory and experimental analysis," *Ultrasonic Imaging*, vol. 1, no. 4, pp. 303–324, Oct. 1979.
- [26] V. Newhouse, N. Bilgutay, J. Saniie, and E. Furgason, "Flaw-to-grain echo enhancement by split-spectrum processing," *Ultrasonics*, vol. 20, no. 2, pp. 59–68, Mar. 1982.
- [27] J. R. Sanchez and M. L. Oelze, "An ultrasonic imaging speckle-suppression and contrast-enhancement technique by means of frequency compounding and coded excitation," *IEEE Trans. on Ultrasonics, Ferroelectrics, and Frequency control*, vol. 56, no. 7, pp. 1327–1339, Jul. 2009.
- [28] J. S. Ullom, M. L. Oelze, and J. R. Sanchez, "Speckle reduction for ultrasonic imaging using frequency compounding and despeckling filters along with coded excitation and pulse compression," *Advances in Acoustics and Vibration*, vol. 2012, p. 16, Apr. 2012, ariticle ID 474039.
- [29] "Ultrasound RF data-set from the Biomedical Ultrasonic Laboratory, University of Michigan," http://www.bme.umich.edu/labs/bul/image_data, 2005, accessed "Aug., 2013".
- [30] J. Fessler, "Reflection-mode ultrasound imaging," <http://web.eecs.umich.edu/~fessler/course/516/l/cu-ultra.pdf>, accessed "Jun., 2013".
- [31] T. Misaridis and J. Jensen, "Use of modulated excitation signals in medical ultrasound," *IEEE Trans. on Ultrasonics, Ferroelectrics and Frequency Control*, vol. 52, no. 2, pp. 177–191, Feb. 2005.

- [32] H. X. Chiao, "Coded excitation for diagnostic ultrasound: A system developer's perspective," *IEEE Trans on Ultrasonics, Ferroelctrics and Frequency Control*, vol. 52, no. 2, pp. 160–170, Feb. 2005.
- [33] B. Ward, A. C. Baker, and V. F. Humphrey, "Nonlinear propagation applied to the improvement of resolution in diagnostic medical ultrasound," *Journal of the Acoustical Society of America*, vol. 101, no. 1, pp. 143–154, Mar. 1997.
- [34] F. A. Duck, "Nonlinear acoustics in diagnostic ultrasound," *Ultrasound in Medicine and Biology*, vol. 28, no. 1, pp. 1–18, Jan. 2002.
- [35] K. Y. Hung, P. H. Wu, T. W. Tsai, and D. C. Shye, "Application of Fresnel equations to improve interface reflection of incline exposure and develop micro-mirros for blu-ray DVDs," in *Industrial Techniology, IEEE Conference on*, vol. 1, VIC, Australia, Feb. 2009, pp. 1–6.
- [36] L. Ferrari and J. P. Jones, "The propagation of Gaussian modulated pulses in dissipative and/or dispersive media such as tissue," *Ultrasound in Medicine and Biology*, vol. 2, no. 11, pp. 299–305, Mar. 1985.
- [37] K. K. Win, J. Wang, C. S. Zhang, and R. Yang, "Identification and removal of reverberation in ultrasound imaging," in *IEEE Conference on Industrial Electronics and Applications*, Taichung, 2010, pp. 1675–1680.
- [38] N. E. Bylund, M. Andersson, and H. Knutsson, "Interactive 3D filter design for ultrasound artifact reduction," in *Image Processing, 2005 IEEE International Conference on*, vol. 3, Italy, Sep. 2005, pp. 728–731.
- [39] G. Treece, R. Prager, and A. Gee, "Ultrasound attenuation measurement in the presence of scatterer variation for reduction of shadowing and enhancement," *IEEE Trans. on Ultrasonics, Ferroelctrics and Frequency Control*, vol. 52, no. 12, pp. 2346–2360, Dec. 2005.
- [40] P. C. Tay, S. T. Acton, and J. Hossack, "A transform method to remove ultrasound artifacts," in *IEEE Southwest Symposium on Image Analysis and Interpretation*, Denver, CO, 2006, pp. 110–114.
- [41] J. Park, J. B. Kang, J. H. Chang, and Y. Yoo, "Speckle reduction techniques in medical ultrasound imaging," *Biomedical Engineering Letters*, vol. 4, no. 1, pp. 32–40, Mar. 2014.

- [42] L. D. Marchi, N. Testoni, and N. Speciale, "Prostate tissue characterization via ultrasound speckle statistics," in *Signal Processing and Information Technology, 2006 IEEE International Symposium on*, Vancouver, BC, Aug. 2006, pp. 208–211.
- [43] B. F. Osmanski, J. Bercoff, G. Montaldo, T. Loupas, M. Fink, and M. Tanter, "Cancellation of Doppler intrinsic spectral broadening using ultrasfast doppler imaging," *IEEE Trans. on ultrasonics, ferroelectrics, and frequency control*, vol. 61, no. 8, pp. 1396–1408, Aug. 2014.
- [44] A. Constant and W. M. D. Wright, "Estimation of tissue elasticity by image processing of simulated B-mode ultrasound images," in *Signals and Systems Conference 2009, IET Irish*, vol. 1, Dublin, Jun. 2009, pp. 10–11.
- [45] M. A. Averkiou, "Tissue harmonic imaging," in *Ultrasonics Symposium, 2000 IEEE*, vol. 2, San Juan, Oct. 2000, pp. 1563–1572.
- [46] S. A. I. Avanji, A. Mahloojifar, and B. M. Asl, "Adaptive 3D MV beam-forming in medical ultrasound imaging," in *Iranian Conference on Biomedical Engineering, 2013*, Tehran, Iran, Dec. 2013, pp. 81–86.
- [47] S. Holm and H. X. Yao, "Improved framerate with synthetic transmit aperture imaging using prefocused subapertures," in *Ultrasonics Symposium, 1997 IEEE*, vol. 2, Toronto, Ont., Oct. 1997, pp. 1535–1538.
- [48] J. A. Jensen, S. I. Nikolov, K. L. Gammelmark, and M. H. Pedersen, "Synthetic aperture ultrasound imaging," *Ultrasonics*, vol. 44, no. 1, pp. 5–15, Dec. 2006.
- [49] G. Montaldo, M. Tanter, J. Bercoff, N. Benech, and M. Fink, "Coherernt plane-wave compounding for very high frame rate ultrasonography and transient elastography," *IEEE Trans. on Ultrasonics, Ferroelectrics and Frequency Control*, vol. 56, no. 3, pp. 489–506, Mar. 2009.
- [50] S. A. Vorobyov, "Principles of minimum variance robust adaptive beamforming design," *Signal Processing*, vol. 93, no. 12, pp. 3264–3277, Dec. 2012.
- [51] T. J. Shan and T. Kailath, "Adaptive beamforming for coherent signals and interference," *IEEE Trans. on acoustics, speech and signal processing*, vol. 33, no. 3, pp. 527–536, Jun. 1985.

- [52] ——, “Adaptive beamforming with the generalized sidelobe canceller in the presence of array imperfections,” *IEEE Trans. on antennas and propagation*, vol. 34, no. 8, pp. 996–1012, Aug. 1986.
- [53] J. Li, P. Stoica, and Z. Wang, “On robust capon beamforming and diagonal loading,” *IEEE Trans. on Signal Processing*, vol. 51, no. 7, pp. 1702–1715, Jul. 2003.
- [54] J. F. Synnevåg, A. Austeng, and S. Holm, “Minimum variance adaptive beamforming applied to medical ultrasound imaging,” in *Ultrasonics Symposium, 2005*, Netherland, Sep. 2005, pp. 1199–1202.
- [55] S. A. Vorobyov, H. Chen, and A. B. Gershman, “On the relationship between robust minimum variance beamformers with probabilistic and worst-case distortionless response constraints,” *IEEE Trans. on signal processing*, vol. 56, no. 11, pp. 5719–5724, Nov. 2008.
- [56] M. Ruebsamen and A. B. Gershman, “Robust adaptive beamforming using multi-dimensional covariance fitting,” *IEEE Trans. on signal processing*, vol. 60, no. 2, pp. 750–753, Feb. 2012.
- [57] B. M. Asl and A. Mahloojifar, “Eigenspace-based minimum variance beamforming applied to medical ultrasound imaging,” *IEEE Trans. on ultrasonics, ferroelectrics and frequency control*, vol. 57, no. 11, pp. 2381–2390, Nov. 2010.
- [58] ——, “Contrast enhancement and robustness improvement of adaptive ultrasound imaging using forward-backward minimum variance beamforming,” *IEEE Trans. on ultrasonics, ferroelectrics and frequency control*, vol. 58, no. 4, pp. 858–867, Apr. 2011.
- [59] J. F. Synnevåg, A. Austeng, and S. Holm, “High frame-rate and high resolution medical imaging using adaptive beamforming,” in *Ultrasonics Symposium, 2006*, Vancouver, BC, Oct. 2006, pp. 2–6.
- [60] S. L. Wang and P. C. Li, “High frame rate adaptive imaging using coherence factor weighting and the MVDR method,” in *Ultrasonics Symposium, 2008*, Beijing, Nov. 2008, pp. 1175–1178.
- [61] I. K. Holfort, F. Gran, and J. A. Jensen, “Plane wave medical ultrasound imaging using adaptive beamforming,” in *Sensor Array and Multichannel Signal Processing Workshop, 2008, 5th IEEE*, Darmstadt, Jul. 2008, pp. 288–292.

- [62] J. F. Synnevåg, A. Austeng, and S. Holm, “A low-complexity data-dependent beamformer,” *IEEE Trans. on ultrasonics, ferroelectrics and frequency control*, vol. 57, no. 2, pp. 281–289, Feb. 2011.
- [63] B. M. Asl and A. Mahloojifar, “A low-complexity adaptive beamformer for ultrasound imaging using structured covariance matrix,” *IEEE Trans. on ultrasonics, ferroelectrics and frequency control*, vol. 59, no. 4, pp. 660–667, Apr. 2012.
- [64] L. Cohen, “Generalization of the Wiener-Khinchin theorem,” *Signal Processing Letters*, vol. 5, no. 11, pp. 292–294, Nov. 1998.
- [65] P. S. Naidu, *Sensor Array Signal Processing*. Florida: CRC Press, 2001.
- [66] C. Burckhardt, “Speckle in ultrasound B-mode scans,” *IEEE Trans. on Sonics Ultrason.*, vol. 25, no. 1, pp. 1–6, Jan. 1978.
- [67] S. K. Jespersen, J. E. Wilhjelm, and H. Sillesen, “Multi-angle compound imaging,” *Ultrasonic Imaging*, vol. 20, no. 2, pp. 81–102, Apr. 1998.
- [68] G. E. Trahey, S. W. Smith, and O. T. von Ramm, “Speckle pattern correlation with lateral aperture translation: experimental results and implications for spatial compounding,” *IEEE Trans. Ultrasonics, Ferroelectrics, and Frequency Control*, vol. 33, pp. 257–264, May. 1986.
- [69] A. R. Groves and R. N. Rohling, “Two-dimensional spatial compounding with warping,” *Ultrasound Med. Biol.*, vol. 30, no. 7, pp. 929–942, Jul. 2004.
- [70] S. M. Gelbach and F. G. Sommer, “Frequency diversity speckle processing,” *Ultrasonic imaging*, vol. 9, pp. 92–105, Apr. 1987.
- [71] V. L. Newhouse, N. M. Bilgutay, J. Saniie, and E. S. Furgason, “Flaw-to-grain echo enhancement by split spectrum processing,” *Ultrasonic imaging*, vol. 4, pp. 59–68, Mar. 1982.
- [72] S. Song, C. H. Yoon, G. D. Kim, and Y. Yoo, “Adaptive frequency compounding for speckle reduction,” in *Ultrasonics Symposium, 2011 IEEE*, Orlando, FL, Oct. 2011, pp. 1435–1438.
- [73] G. Gunarathne, *Advancements and Breakthroughs in Ultrasound Imaging*. NJ, USA: InTech, 2013.

- [74] M. S. Patterson and F. S. Foster, “The improvement and quantitative assessment for B-mode images produced by an angular array/cone hybrid,” *Ultrason. Imaging*, vol. 5, no. 3, pp. 195–213, Jul. 1983.
- [75] J. F. Synnevåg, C. I. C. Nilsen, and S. Holm, “Speckle statistics in adaptive beamforming,” in *IEEE Ultrasonics Symposium*, New York, USA, Oct. 2007, pp. 1545–1548.